



BRNO UNIVERSITY OF TECHNOLOGY

VYSOKÉ UČENÍ TECHNICKÉ V BRNĚ

FACULTY OF MECHANICAL ENGINEERING

FAKULTA STROJNÍHO INŽENÝRSTVÍ

INSTITUTE OF PHYSICAL ENGINEERING

ÚSTAV FYZIKÁLNÍHO INŽENÝRSTVÍ

X-RAY COMPUTED TOMOGRAPHY ANALYSIS OF MOUSE EMBRYONIC HEART

ANALÝZA SRDCE MYŠÍHO EMBRYA PROSTŘEDNICTVÍM RENTGENOVÉ POČÍTAČOVÉ TOMOGRAFIE

MASTER'S THESIS

DIPLOMOVÁ PRÁCE

AUTHOR

AUTOR PRÁCE

Bc. Daniela Dobrovodská

SUPERVISOR

VEDOUCÍ PRÁCE

Ing. Tomáš Zikmund, Ph.D.

BRNO 2021

Assignment Master's Thesis

Institut: Institute of Physical Engineering
Student: **Bc. Daniela Dobrovodská**
Degree programm: Applied Sciences in Engineering
Branch: Precise Mechanics and Optics
Supervisor: **Ing. Tomáš Zikmund, Ph.D.**
Academic year: 2020/21

As provided for by the Act No. 111/98 Coll. on higher education institutions and the BUT Study and Examination Regulations, the director of the Institute hereby assigns the following topic of Master's Thesis:

X–ray computed tomography analysis of mouse embryonic heart

Brief Description:

X–ray computed tomography has been gradually becoming one of the go–to methods for the precise 3D analysis of biological samples in various fields of biological research. Specifically, in developmental biology research where the model organisms are small embryos, the high resolution CT devices bring new opportunity to analyze even the smallest details. Rigaku nano 3DX is one of these high–resolution devices able to scan the samples in sub–micron resolution and the specific setup of this device allows to apply phase–contrast imaging. The developing heart is a compact organ mainly composed of the myocardium with a few other supporting cell types, including intra–cardiac neuronal populations referred to as parasympathetic ganglia. A variety of genetic alterations in the mouse can lead to cardiac phenotypes that cannot be detected on the macroscopical level, such as the collective orientation and dimensions of individual muscle fibres. In such cases, these phenotypes can only be unravelled using high–resolution imaging techniques, such as micro and nano CT. The objective of this work will be to determine the optimal imaging methodology for the mouse embryonic heart by CT including determination of proper staining agent and comparison of results from phase contrast and absorption contrast imaging and finally validation of the results by confocal microscopy. The procedure for quantification of differences in wild type mice and mutants with potential cardiac phenotype will be introduced.

Master's Thesis goals:

- study the literature sources regarding staining of the soft tissues and principles of phase–contrast imaging
- selection of proper staining agent for the mouse hearts and optimization of the staining procedure
- performing measurements of selected samples on Rigaku nano3DX
- application of phase–contrast imaging to the obtained data
- evaluation of obtained data, design of data analysis
- volumetric analysis of:
 1. the four chambers of the heart (atria, ventricles – both inner cavity and muscle wall)
 2. total cardiac muscle (ventricular and atrial myocardium)
 3. ventricular septum
- comparison of obtained nano CT data with data from a confocal microscope

Recommended bibliography:

KALASOVA, Dominika, Tomas ZIKMUND, Ladislav PINA, Yoshihiro TAKEDA, Martin HORVATH, Kazuhiko OMOTE a Jozef KAISER, 2020. Characterization of a Laboratory-Based X-Ray Computed Nanotomography System for Propagation-Based Method of Phase Contrast Imaging. IEEE Transactions on Instrumentation and Measurement [online]. 69(4), 1170-1178 [cit. 2020-10-14]. ISSN 0018-9456. Dostupné z: doi:10.1109/TIM.2019.2910338

METSCHER, Brian D, 2009. MicroCT for comparative morphology: simple staining methods allow high-contrast 3D imaging of diverse non-mineralized animal tissues. BMC Physiology [online]. 9(1) [cit. 2020-10-14]. ISSN 1472-6793. Dostupné z: doi:10.1186/1472-6793-9-11

METSCHER, Brian D., 2009. MicroCT for developmental biology: A versatile tool for high-contrast 3D imaging at histological resolutions. Developmental Dynamics [online]. 238(3), 632-640 [cit. 2020-1-14]. ISSN 10588388. Dostupné z: doi:10.1002/dvdy.21857

Deadline for submission Master's Thesis is given by the Schedule of the Academic year 2020/21

In Brno,

L. S.

prof. RNDr. Tomáš Šikola, CSc.
Director of the Institute

doc. Ing. Jaroslav Katolický, Ph.D.
FME dean

Abstract

X-ray computed tomography is a versatile technique allowing non-destructive three-dimensional (3D) imaging. It is widely used in industry for metrology and material characterisation. Lately, it has found its importance also in biology and developmental science, where the 3D reconstructed data provide more comprehensive information about the sample than the conventional 2D imaging methods. Moreover, it can produce high-quality images of various biological samples. The obstacle in imaging biological samples might be a very similar attenuation coefficient of soft tissue, and therefore staining with chemical substance must be used. This thesis aims to use microcomputed tomography to visualise and qualitatively evaluate embryonic mouse hearts E17.5 and introduce the best staining protocol. Furthermore, the methodology for highlighting differences between wild type mice and mutant is introduced. Rigaku nano 3DX is used for the experiments with mouse heart interventricular septum, and after considering the specific setting of the device, the phase retrieval algorithm is applied. Finally, the validation of the μ CT data is performed by comparing pictures from the confocal microscope.

Abstrakt

Rentgenová počítačová tomografie je univerzální technika umožňující nedestruktivní trojrozměrné (3D) zobrazování. Je široce používána v průmyslu pro metrologii a charakterizaci materiálů. V poslední době našla svůj význam také v biologii a vývojové vědě, kde 3D rekonstruovaná data poskytují komplexnější informace o vzorku než konvenční 2D zobrazovací metody. Kromě toho může vytvářet vysoce kvalitní snímky různých biologických vzorků. Překážkou při zobrazování biologických vzorků může být velmi podobný koeficient útlumu měkkých tkání, a proto je nutné použít barvení chemickou látkou. Tato práce si klade za cíl pomocí mikropočítačové tomografie vizualizovat a kvalitativně vyhodnotit srdce embryonálních myší E17.5 a představit nejlepší barvicí protokol. Dále je představena metodika pro zvýraznění rozdílů mezi myší divokého typu a mutantem. Rigaku nano 3DX je použit pro experimenty s mezi-komorovou přepážkou myšího srdce a po nastavení specifických parametrů zařízení je použit algoritmus pro zvýraznění fáze. Nakonec je provedena validace μ CT dat se snímkami z konfokálního mikroskopu.

Keywords

computed tomography, image processing, 3D imaging, mouse heart, phase contrast

Klíčová slova

počítačová tomografie, zpracování obrazu, 3D zobrazování, myší srdce, fázový kontrast

DOBROVODSKÁ, Daniela. *X-ray computed tomography analysis of mouse embryonic heart*. Brno, 2021. Master's thesis. Brno University of Technology, Faculty of Mechanical Engineering, Institute of Physical Engineering. Supervised by Tomáš Zikmund.

Prohlašuji, že jsem diplomovou práci *Analýza srdce myšního embrya prostřednictvím rentgenové počítačové tomografie* vypracovala samostatně pod vedením Ing. Tomáše Zikmunda, Ph.D., s použitím materiálů uvedených v seznamu literatury.

I declare that I have elaborated my master's thesis *X-ray computed tomography analysis of mouse embryonic heart* independently, under the supervision of Mgr. Tomáš Zikmund, Ph.D. All sources used or excerpted during the elaboration of this work are properly cited and listed in the references.

Bc. Daniela Dobrovodská

Ráda bych poděkovala mému vedoucímu Ing. Tomáši Zikmundovi, Ph.D., za cennou pomoc a rady, které mi při práci poskytl. Dále bych ráda poděkovala Marii Eleni Kastriti, Ph.D. a Mgr. Michaelae Kavkové za pomoc s přípravou embryí a při kontrastování vzorků. Na závěr bych ráda poděkovala celé výzkumné skupině CTLAB na CEITEC za pomoc a hlavně obětavost během náročného období.

Bc. Daniela Dobrovodská

Contents

| | |
|---|-----------|
| Introduction | 3 |
| 1 X-ray computed tomography | 5 |
| 1.1 Röntgen radiation | 5 |
| 1.2 Computed Tomography | 6 |
| 1.3 X-ray tube | 6 |
| 1.4 X-ray matter interaction | 8 |
| 1.5 Image reconstruction technique | 9 |
| 1.5.1 Projections and Radon transform | 10 |
| 1.5.2 The Fourier Slice Theorem | 10 |
| 1.5.3 Filtered Back-Projection | 11 |
| 2 Imaging of biological samples | 15 |
| 2.1 Conventional methods | 15 |
| 2.1.1 Confocal microscopy | 15 |
| Fluorescent confocal microscopy | 17 |
| Differential interference contrast mode | 17 |
| 2.1.2 Light Sheet Microscopy | 19 |
| 2.2 3D imaging with CT | 20 |
| 2.2.1 Contrast enhancing in soft tissue | 21 |
| 2.3 Imaging in phase-contrast | 22 |
| 2.3.1 Phase-contrast imaging methods | 22 |
| Crystal Interferometer Method | 22 |
| Talbot Interferometer Method | 23 |
| Diffraction Enhanced Imaging | 25 |
| In Line Method | 25 |
| 3 Experimental part | 29 |
| 3.1 Introduction | 29 |
| 3.2 Materials and Methods | 30 |
| 3.2.1 Sample preparation | 30 |
| 3.2.2 Histological samples | 30 |
| 3.2.3 Samples for Computed Tomography | 32 |
| 3.2.4 Measurements with μ CT | 33 |
| 3.3 Results | 35 |
| 3.3.1 Image quality evaluation | 35 |
| 3.3.2 Processing of the data | 40 |
| Anatomy and physiology | 40 |

| | | |
|-------|--|-----------|
| | Segmentation | 41 |
| 3.3.3 | Analysis of 3D models | 43 |
| | Volumetric analysis | 43 |
| | Wall thickness analysis | 44 |
| | Nano CT evaluation of the heart septum | 46 |
| 3.3.4 | Validation of the tomographic data with CLSM | 51 |
| 3.3.5 | Example on a mutant and a wild type | 55 |
| | Conclusion | 57 |
| | References | 59 |
| | List of abbreviations and symbols | 67 |

Introduction

Nowadays, genetically manipulated mouse models are widely used for describing many disease processes. Cardiac abnormalities are one of the most common anomalies occurring in newborn babies [1]. Modified mouse models help to understand the mechanism that could regulate human heart development. Therefore, many scientific research is aimed at studying cardiac development and structure [2, 3, 4].

Conventional histological methods are based on cutting tissue into thin slices, which are imaged using a confocal microscope. However, this method is limited with imaging only a thin piece of studied tissue; thus, the complexity of biological structure is lost. On the other hand, the advantage of a confocal microscope is scanning the sample point by point and rejecting out of focus information, thus increasing spatial resolution.

To describe the phenotype in detail, micro-computed tomography (μ CT) is used. This new innovative and highly versatile technique allows non-destructive three - dimensional (3D) imaging. It is commonly used in industry for material characterisation, metrology or geology [5, 6]. Lately, it has become a well-established tool for imaging biological samples where the 3D reconstructed data provide more a comprehensive information about the sample than the conventional 2D imaging method. It can produce high-quality images of various biological samples [7, 8, 9]. The absorption contrast is obtained by different attenuation of the X-ray beam penetrating the sample from different angles. By mathematical reconstruction algorithm, it is possible to acquire 3D information.

Biological samples are mainly composed of soft tissue; therefore, imaging is challenging due to the same attenuation coefficient within the piece. In addition, these specimens absorb X-rays only weakly, and thus staining with chemical substances must be used. Different staining protocols have been proposed varying in contrasting agent, soaking time, biological tissue and size of the sample [10, 11]. The 3D information of the biological structure provided by computed tomography is usually further processed using a segmentation software.

The other way how to improve contrast in weakly absorbing biological tissue is to use its phase-shifting properties. Rigaku Nano3DX is a laboratory nano CT system that is suitable for phase-contrast imaging. The conditions for observing in phase contrast are imaging in the near-field regime with high coherence of the X-ray beam and avoiding geometrical unsharpness. The advantage of this method is a broader accessibility compared to the synchrotron facilities with fully coherent radiation sources [12].

This thesis aims to perform an analysis of a mouse embryonic heart using the abilities of computed tomography. The first two chapters in this work are theoretical; the first chapter discusses the topics related to computed tomography, the discovery of X-rays, the principle of an X-ray tube and the basic principle of the analytical reconstruction method. The second chapter is devoted to different possibilities in imaging biological samples (confocal microscopy and its different imaging modes), the necessity to use stained tissue to accomplish better contrast and different phase-contrast imaging methods. The third chapter is devoted to experimental work - sample preparation, imaging using a confocal microscope and measurements with μ CT. A proper staining agent is selected to increase the absorption contrast of cardiac muscle. The data are evaluated, and 3D models are analysed. Rigaku Nano3DX is used to perform the heart septum measurement, and a phase retrieval algorithm is applied to improve the contrast. The data from the confocal microscope are used for evaluating the accuracy of μ CT. Finally, the hearts of the wild type mice and the mutant are compared.

1. X-ray computed tomography

"Where does this seemingly inconceivable idea come from, this bloodless "cutting" of a person slice by slice, then to reassemble the slices to describe in details the result of this incredible journey deep into the human body [13]."

The invention of X-ray computed tomography enabled us to look inside an object of interest without violating its internal structure. It is a non-invasive high-resolution imaging technique used widely in the medical field for bone or tissue imaging, industry or many other research applications [13].

1.1 Röntgen radiation

Wilhelm Conrad Röntgen was a German scientist who focused his research on light phenomena and other emissions produced by electric discharge in Crookes tubes. Crookes tubes are glass bulbs with cathode and anode, evacuated of air, displaying fluorescent glow by applying high voltage current. On November 8, 1895, he noticed that even though he covered the tube with black cardboard, he could still see the glow on the platinobarium screen placed nine feet (2.74 m) away. From this experiment, he recognised that invisible rays cause this fluorescence. In fact, he did not really understand what these rays are, so he called them X-rays. In 1901 he was awarded the Nobel Prize for Physics for his breakthrough discovery. Further research showed that these rays could penetrate most substances, including the soft tissue of the human body, and therefore, this technique first found its way into the medical field [14].

Almost immediately after Röntgen's discovery, the modern area of medical imaging has started. Doctors started taking images of bones fractures, which helped them to treat injuries more precisely. Soon, this technique was implemented all over the world. Unfortunately, in the early beginnings, there was little knowledge of the potentially harmful effects of ionizing radiation of X-rays [15].

Nowadays, we know that X-rays are part of the electromagnetic spectrum. They have a wavelength in the range of 0.01 nm to 10 nm, corresponding to frequencies in the range of $3 \times 10^{16} - 3 \times 10^{19} \text{ Hz}$ and energies in the range of 100 eV to 100 keV. X-rays have an extremely short wavelength in comparison to visible light. This feature enables them to penetrate through materials that absorb or reflect visible light [15]. X-rays can be divided into "soft" rays with an energy spectrum of 0.12 keV to 12 keV and "hard" rays which have an energy range from 12 keV to 120 keV [16].

The discovery of X-ray radiation was essential but insufficient for the start of com-

puted tomography. It also required the development of computational techniques [13].

1.2 Computed Tomography

Tomography is a technique used for obtaining cross-sectional slice images. The term comes from the Greek word "*tomos*" meaning "*slice*" or "*section*" and "*graphia*" meaning "*describing*" [15]. The main part in the computed tomography invention played two scientists: Allan MacLeod Cormack and Godfrey Newbold Hounsfield. They combined the technology of computers with X-rays and were awarded the Nobel Prize for Physiology and Medicine in 1979 [13]. The era of modern medical imaging did not start before the 1970s. The new method called Computed Tomography or CT was introduced, which provided digital image produced by a computer. The method was sensitive to the tissue density and enabled a cross-sectional view of the human body and, eventually, the 3D view of internal anatomical structures. It improved diagnosis, treatment, guidance, therapy monitoring, and it minimised invasive surgery. Often it is recognised as the most crucial invention in diagnostic radiology [15].

In recent years CT scanning technology has been adapted in advancing high - resolution industrial computed tomography. CT is used in dimensional metrology for non-destructive measurements, material characterisation and measurements of internal structures [17].

In industrial computed tomography scanning, the X-ray dosage is not so crucial as in medicine, where ionization radiation can cause tissue damage and trigger carcinogenesis. Moreover, there is no need to achieve an ultra-fast scan so that higher precision might be achieved. The main interest is to achieve the best possible resolution, accuracy and precision. Another difference is in the rotational component of the scanner. In the industrial CT, the scanning apparatus is fixed, and the sample is rotated, whereas, in medical CT, the patient is stationary, and the scanning apparatus is rotating. The industrial system is more stable and accurate. Most industrial CT scanners use a fan or cone beam of X-rays. Cone beam scanners can gather 3D volumetric data in one rotation by using a 3D cone of X-rays. Fan beam systems acquire slice data, and, therefore, they are slower than the cone beam scanners. On the other hand, fan-beam can produce data with higher accuracy. Detectors in industrial CT use scintillators with charge-coupled devices (CCD) [17].

1.3 X-ray tube

The X-ray tube is used in computed tomography systems as a source of X-rays. Conventional design is made from glass envelope, whereas metal and ceramic tubes are increasingly used nowadays due to the longer life expectancy and higher heat capacity. Inside the tube, there is a negative cathode, consisting of the thin filament, usually tungsten, and a positive anode with a small amount of a tungsten, molybdenum or copper target. The whole tube is placed in protective housing. Electrons are emitted from the cathode by thermionic emission into the vacuum. They are accelerated to-

wards the anode with electric potential, and after hitting anode, they collide with the atoms of a target object, producing X-rays. X-ray radiation requires a vacuum environment to avoid interaction with the gas molecules, which could cause the production of secondary electrons. As a result, about 1 % of the generated energy is converted into X-rays (the rest is radiated as heat) [15, 16].

Two different mechanisms produce x-ray photons - first, Bremsstrahlung ("slowing down") radiation which is detected as continuum spectrum. A positively charged atomic nucleus slows down the negative electron, forcing it to change the path and release energy as X-rays. The energy of the resulting X-rays depends on how close the electron went to the nucleus. The process is creating the whole spectrum of X-ray energies [18].

Second, X-ray fluorescence (or characteristic radiation), creating a line (discrete) spectrum, is caused when the incoming electron collides directly with the targeted atom's inner-shell electron. This electron is ejected from its original place, creating a so-called vacancy and is replaced by an electron from the outer-shell. The loss in potential energy is radiated as an X-ray photon. Most of the X-rays are produced as bremsstrahlung radiation and only a tiny amount as characteristic radiation. The processes are illustrated in Figure 1.1 [19].

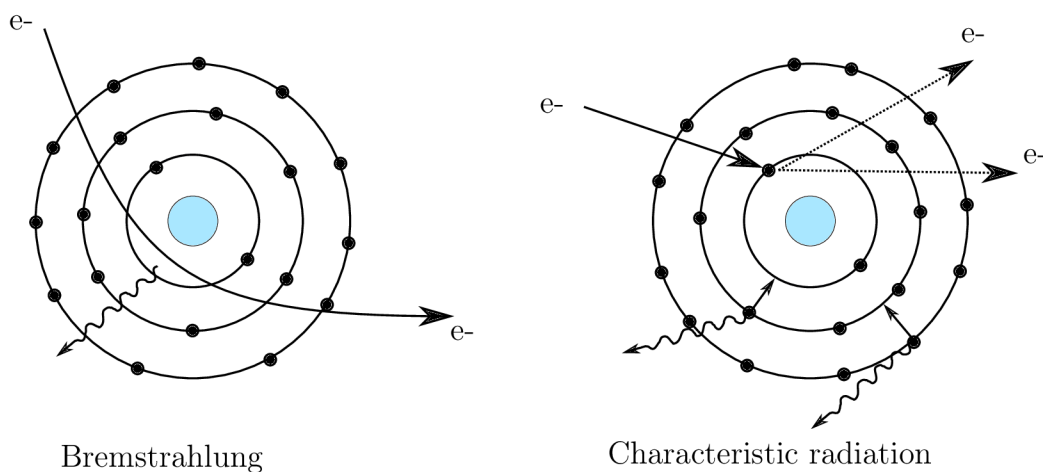


Figure 1.1: Radiation types. Left: Bremsstrahlung radiation, Right: X-ray fluorescence (or characteristic radiation) according to [18].

The efficiency of the X-ray source can be determined by [15]:

- focal spot size (defines the spatial resolution of CT)
- spectrum of X-ray energies (ability to penetrate objects and their attenuation as they pass through different materials with different density)
- intensity of X-rays.

A spectrum of X-ray energies can be adjusted by voltage (by increasing the voltage, the wavelength is decreasing) or installing different filters. The unfiltered X-ray spectrum is composed of "hard" X-rays and "soft" non-penetrating X-rays. Primarily, this

low-energy ("soft") X-rays are more easily attenuated by matter and are responsible for beam hardening artefacts. The beam hardening is thus caused by signal attenuation, which causes an increase in the mean energy of the X-ray beam. The result is an underestimation of the attenuation. Therefore, flat thin metal filters are applied to reduce the effect of low-energy X-rays. These filters are usually made from aluminium, copper or tin. X-ray intensity can be increased by increasing the current flow without changing the X-ray spectrum [15, 16, 17].

Using higher energies leads to better and easier X-rays' penetration ability, but on the other hand, higher energies cause reduced sensibility to changes in material density and compositions. To conclude, intensity affects the signal-to-noise ratio and, therefore, the image quality [15].

Conventional laboratory X-ray sources are polychromatic or polyenergetic - emitted photons have a broad spectrum of energies. For the practical applications are preferred monochromatic or monoenergetic X-ray sources. Nearly monochromatic sources are made at synchrotron facilities. However, these systems are large and expensive [19, 20].

1.4 X-ray matter interaction

The X-ray beam passes through an object and is attenuated by absorption or scattered. The degree of attenuation depends on the X-ray's energy spectrum, atomic number and mass density of the penetrated specimen. The process of attenuation can be characterised by Beer-Lambert law (for the homogeneous object using monochromatic radiation):

$$I_t = I_0 \exp(-x\mu) \quad (1.1)$$

where I_0 and I_t are incident and transmitted beam intensities, respectively, x is the length of X-ray path, μ is X-ray linear attenuation coefficient (it depends on the type of the material of the specimen) [15, 19]. In computed tomography, the fraction I_t/I_0 is used to measure a ray path through the object. The logarithm of this ratio is used for getting line integrals which are essential for image reconstruction described in Chapter 1.5 [18].

When considering an inhomogeneous object, factor $\mu(x)$ is a linear attenuation coefficient at each point on the ray path. In practice, X-ray photons have various energies; the beam is polychromatic, so the attenuation coefficient also depends on energy.

$$I_t = \int_0^{E_{max}} I_0(E) \exp\left(-\int \mu(x,E) dx\right) dE \quad (1.2)$$

where $I_0(E)$ is normalised energy spectrum [18].

Three mechanisms dominate the attenuation:

- Coherent (Rayleigh) scatter
- Photoelectric absorption

- Compton scatter

The effect of the first two is related to the atomic number Z . The tissue is mainly composed of low atomic elements; therefore, the most significant attenuation is done by Compton scattering [19].

Rayleigh scattering is a coherent process with low X-ray energies. Low energy interaction does not cause orbital electrons' ejection, but the whole atom is set to vibration. In this process, no ionization occurs, and no energy is converted to kinetic energy. The contribution of Rayleigh scattering to attenuation is smaller in comparison to other effects [18].

The photoelectric effect was described by Albert Einstein. It accounts for an event where incident X-ray photon energy is more significant than an inner-shell electron's binding energy. The electron (referred to as photoelectron) is ejected from its previous position. An outer shell electron fills the "hole" with higher energy, so characteristic radiation occurs. Thus the result of this process is a positive ion, a photoelectron and a photon of characteristic radiation [18].

Compton scattering is the dominant type of scattering mechanism for the high X-ray energies in tissue-like materials. In this case, the energy of incident X-rays is considerably higher than the electron's binding energy; thus, the electron is ejected from the atom. The incoming light is deflected with partial loss of its energy used for the ejected electron (Compton electron). Therefore, the interaction produces a positive ion, Compton electron and a scattered photon [18].

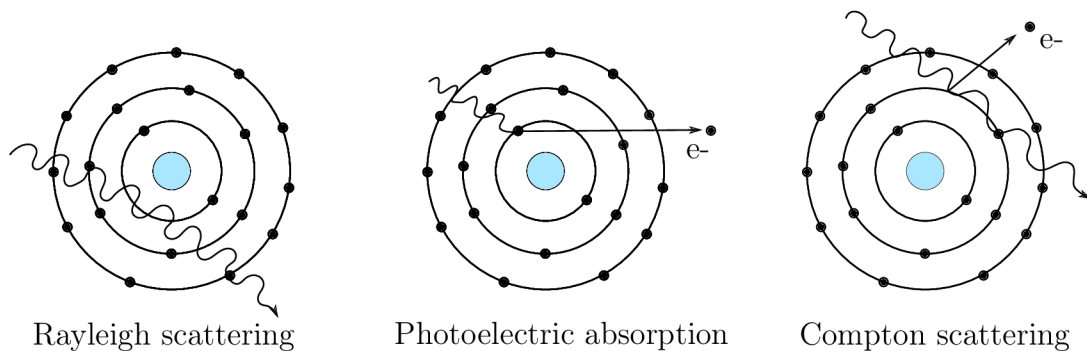


Figure 1.2: Attenuation mechanisms. Left: Rayleigh scattering, Middle: Photoelectric absorption, Right: Compton scattering according to [18].

1.5 Image reconstruction technique

Image reconstruction can be classified into analytical, algebraic and statistical algorithms. Conventional analytical reconstruction, described in the following chapter, represents the object as a mathematical function, reconstructing the object by solving a continuous integral equation [17].

1.5.1 Projections and Radon transform

Image reconstruction in computed tomography is a mathematical process that generates tomographic images from obtained X-rays projections. Projections are X-ray images generated by attenuated X-rays passing through the rotating object. Each pixel on the detector can be represented by a line integral describing X-ray attenuation coefficients along the straight line travelling through the object [21, 22].

The goal is to estimate the distribution of the linear attenuation coefficient along the projection line and reconstruct the original image. These mathematical steps are the most crucial parts of the CT imaging process. Moreover, they are important for the final image quality. In the simplest mathematical explanation the object is described as 2D function $f(x,y)$. Parallel X-rays pass through the object and form a projection image $p(s,\theta)$ on the detector. A projection is composed of a set of line integrals while each is described by the s, θ parameters [22].

The Radon transform turns the image function values $f(x,y)$ into the line integral values $p(s,\theta)$. Therefore, the inverse Radon transform is used during the CT reconstruction to obtain images from the line integrals.

The Radon transform of the image function $f(x,y)$ is given by,

$$p(s,\theta) = \int_{-\infty}^{\infty} \int_{-\infty}^{\infty} f(x,y) \delta(x \cos \theta + y \sin \theta - s) dx dy \quad (1.3)$$

where δ is Dirac's δ -function used to select the object parts that are illuminated by X-rays. This function has zero values everywhere except for the zero, where it goes to infinity [22].

This process is schematically visualised in Figure 1.4. As an example, it is used a model picture (first image). By taking a Radon transform from the model picture loaded in Matlab, we obtain a projection. After using the function: inverse Radon transform, on previously obtained projection, we get so-called back-projection (smeared image). After repeating this process from different angles and summing all back-projections together, we obtain the original image. In this example, projections are taken every 10° over 180° . The process has some imperfections - the halo effect, which can be seen in blurred edges. The mathematical principle of avoiding this negative artefact will be described in the chapter 1.5.3.

1.5.2 The Fourier Slice Theorem

The Fourier Slice Theorem can be derived by taking the 1-D FT of a projection and noting that it is equal to a slice of the 2-D FT of the original object, schematically labelled in picture 1.3 [22].

The 1-D FT of projection $p(s,\theta)$ is defined as:

$$P(\omega,\theta) = \int_{-\infty}^{\infty} p(s,\theta) \exp(-i2\pi\omega s) ds \quad (1.4)$$

Deriving the equation, and substituting the $p(s,\theta)$ with Radon transform (equation

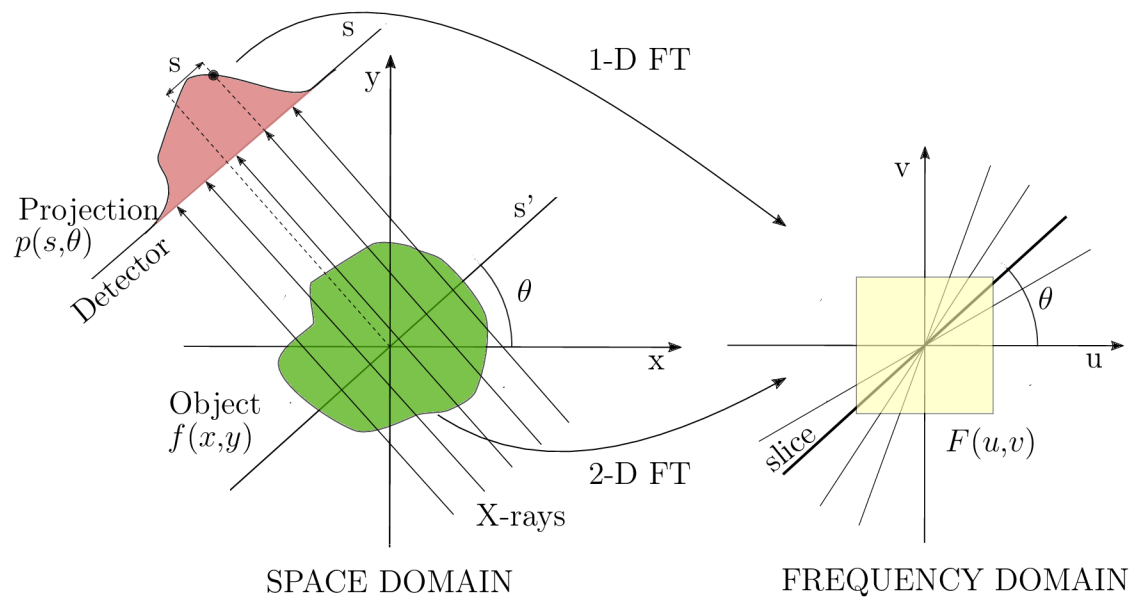


Figure 1.3: Left: X-rays passing through the object, creating a projection image at the detector. Right: After 1-D FT, it can add one slice image to reconstructing the image. Picture according to [22].

1.3), can be obtained the following equation, which is the 2-D FT through the object $f(x,y)$:

$$F(u,v) = \int_{-\infty}^{\infty} \int_{-\infty}^{\infty} f(x,y) \exp(-i2\pi(ux + vy)) dx dy \quad (1.5)$$

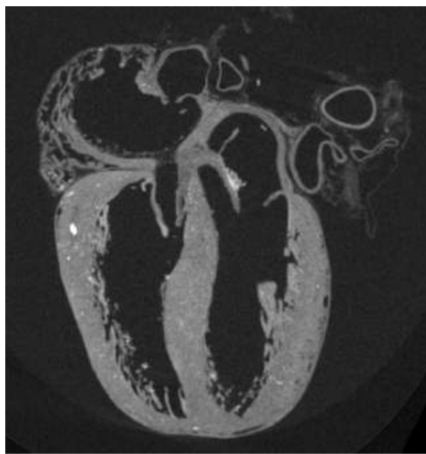
where $u = \omega \cos \theta$ and $v = \omega \sin \theta$.

Every time the projection is taken, a new slice is added to the reconstructing image. The Fourier Slice Theorem provides a simple model for understanding tomographic reconstruction, but in practice, different approaches are being used [22].

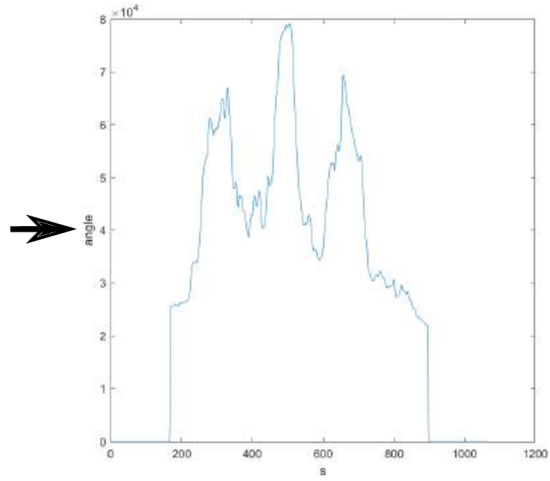
1.5.3 Filtered Back-Projection

The most commonly used reconstruction algorithm is filtered back-projection (FBP). The popularity of the FBP method is because of its computational efficiency and numerical stability [22].

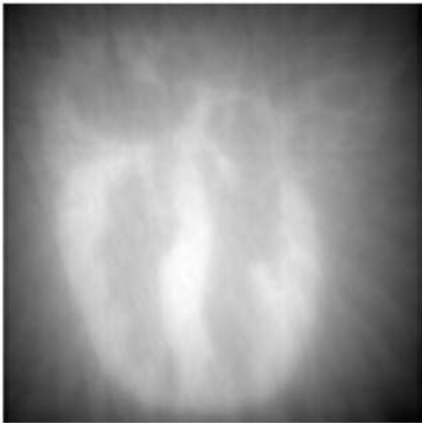
Each projection represents a nearly independent measurement of the object. Reconstruction is the sum of projections of the object. This summation can be done in the space domain or frequency domain. Reconstruction can be divided into two parts: Filtering and Back-projection. Back-projection resembles the inverse operation of forward projection. The result of this process is a smeared image = back projection. The original image is created by summing up each back-projection. The problem that the image is blurred is due to the Fourier Slice Theorem. In the frequency domain, the object is sampled so that low frequencies are present more often than high frequencies (Figure 1.5). In image processing, the low frequencies take care of the smooth surface,



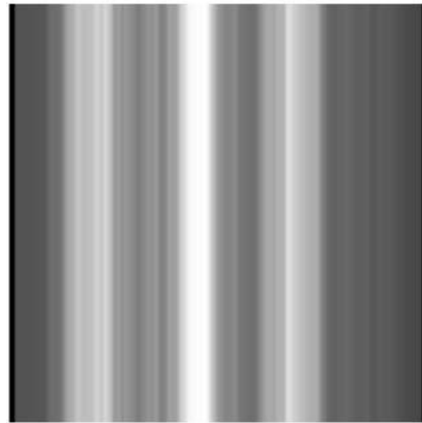
1. model picture



2. projection



4. backprojections
summed together



3. backprojection

Figure 1.4: 1. the model image, 2. Radon transform of the model picture, 3. Inverse Radon transform from the projection, 4. reconstruction of the original image.

and on the other hand, high frequencies are responsible for the details and sharp edges. Missing high frequencies cause blurry edges [22].

In order to reduce the oversampling by low frequencies, filtering is required. The equation for filtered back-projection is derived from inverse 2-D FT of function $F(u,v)$ (equation 1.5) while changing coordinates to polar [22]. The equation is:

$$f(x,y) = \int_0^\pi \int_{-\infty}^\infty |\omega| F(\omega \cos \theta, \omega \sin \theta) \exp(i2\pi(x \cos \theta + y \sin \theta)\omega) d\omega d\theta \quad (1.6)$$

where $|\omega|$ is filter function.

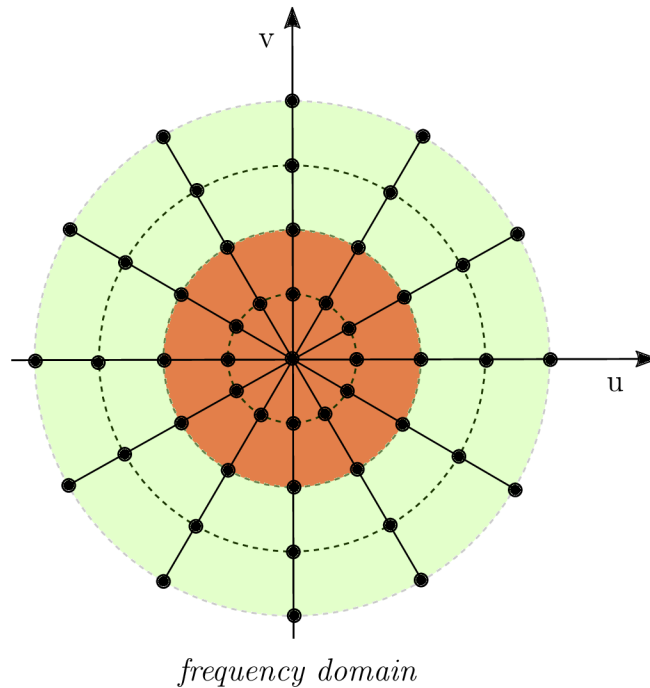


Figure 1.5: Frequency sampling in the Fourier frequency domain. Red colour: low frequencies, Green colour: high frequencies [22].

In the FBP algorithm the focal spot is considered to be a point and radiation is monochromatic. These approximations in calculation might effect the quality of reconstruction. Therefore, iterative reconstructions are used to overcome these problems. Algebraic reconstruction techniques use several iterations which are performed until certain criteria are met. Statistical techniques use also iterative methods, but here the unknowns are assigned by means of likelihood principles. Iterative techniques require more time for computation than analytical algorithms. On the other hand these methods reconstruct better quality images. [17].

2. Imaging of biological samples

2.1 Conventional methods

Light microscopy is undoubtedly the most common technique for imaging and observing biological samples using visible light to produce an image of an object. The non-invasive property of visible light allows studying living cells, tissues and microorganisms. In the microscope, the objective and the eyepiece work together to produce the final magnified image. A wave of light interacting with an object changes in either amplitude or phase. The human eye can only distinguish amplitude and wavelength difference, not the phase shift. Optical microscopes use different light contrasting techniques and a wide variety of labelling to highlight structures and components of the sample. Bright-field and dark-field microscopy is a simple illumination technique based on contrast due to differences in wave amplitudes. Sample appears black in a white background or white in a dark background for bright-field and dark-field, respectively. However, most of the biological samples are phase objects with low absorption contrast, which do not absorb light but they slightly alter the phase of light. Some of the contrast-improving techniques are phase contrast, polarized light or differential interference contrast (DIC). Fluorescence is by far the most widely used light-contrast technique. The advantages are to label individual structures, molecules, cells, even to study the dynamic of the living cells or to identify several molecules simultaneously [23, 24].

In a conventional wide-field microscope, by focusing the objective at a specific focal plane, the specimen's entire depth is illuminated, and most of the light is collected, even the light from out-of-focus. This out-of-focus light reduces contrast and resolution [25, 26]. The next chapter is devoted to confocal microscopy and its different imaging modes, which are frequently used in biology for a wide variety of cell research to describe the complexity of the morphology and dynamics of cells and tissue.

2.1.1 Confocal microscopy

The term "confocal" refers to the fact that the illumination, specimen and detection system are focused on the same spot. The confocal microscope uses pinholes at the illumination and detection planes to scan sample point by point in the x and y directions [25, 26].

The main improvement in confocal microscopy was the fact that out-of-focus light was eliminated with the illumination focused in a small spot, and thus, it was able to

increase spatial resolution. Spatial resolution is further divided into lateral and axial resolution [25, 26]. Lateral resolution is defined as:

$$d_{xy} = \frac{0.4\lambda}{NA} \quad (2.1)$$

λ is wavelength and NA is numerical aperture defined as $NA = n \sin \alpha$, where n is refractive index and α is aperture angle.

The axial resolution of a confocal system is:

$$d_z = \frac{1.4n\lambda}{NA^2} \quad (2.2)$$

The diameter of the pinhole controls spatial resolution. The limit for the resolution is set by diffraction limit; thus, the optimum pinhole value is considered at the full width at half maximum intensity (FWHM) of the Airy disk. This coincides with 75 % of its intensity passing through the system. Dimmer rings of light are blocked from detection. If the pinhole is bigger than an Airy disk, the resolution response to a wide-field microscope [25, 26].

The resulting image is taken from one desired plane of focus. This principle of "cutting" the specimen is often referred to as "optical knife". Optical sections of the specimen can be taken in different planes (xy - perpendicular to the optical axis, xz, yz). Obtaining 3D images from the specimen is done by acquiring more optical sections taken along z axis (Z-series). 3D reconstruction is obtained by reconstruction software by precisely stacking the 2D optical sections [25, 26].

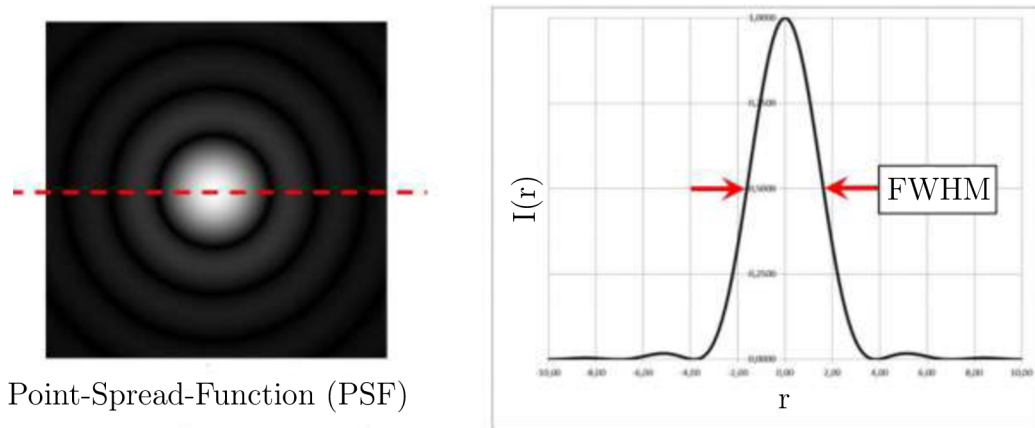


Figure 2.1: Left: point spread function by a circular aperture with an inner spot - Airy disc. Right: profile through the Airy disc, red arrows label FWHM [27].

Confocal laser scanning microscope (CLSM) uses as a source of light lasers providing high brightness, low noise and low beam divergence and can be very easily focused into a small spot. The most common lasers are air-cooled or water-cooled argon ion lasers, krypton-argon ion lasers, helium-neon lasers, helium-cadmium lasers, UV lasers, and infrared lasers. New generation CLSMs use a combination of lasers. The disadvantage

is the limitation in used wavelengths (available by lasers). Detectors used in confocal microscope are: a photo-multiplier tube (PMT), avalanche photodiodes (APD) or a charge-coupled device (CCD) camera. [25, 26].

Confocal laser scanning microscopy can operate in various modes; for instance, CLSM is closely connected with fluorescent imaging in biomedical application. Furthermore, for the precise location of labelled cells within a tissue, transmitted light imaging modes are used (phase-contrast, differential interference contrast, dark-field, polarised light). The transmitted light images and confocal fluorescence images can be acquired simultaneously using the same illumination beam [25, 26].

Fluorescent confocal microscopy

Fluorescent microscopy uses fluorescence principles which are very common in biological imaging. Combining this technique with laser scanning confocal microscopy provides excellent results.

The energy level structure of each molecule determines the wavelength of absorbed or emitted light. The molecule absorbs light (excitation wavelength) and gets from the ground state to an excited state. After a short period, the molecule releases part of its energy as fluorescence radiation (emission wavelength). Fluorescent light is always at longer wavelengths (less energy) than excitation light. The process is illustrated in Figure 2.2. The loss of energy is called Stokes shift (peak shift of excitation to emission state) shown in Figure 2.3. Each fluorescent dye has a specific excitation spectrum. Multiple fluorescent dyes can be used simultaneously on a biological sample (usually 3-4 fluorescent dyes). Fluorescent emission F can be expressed as $F = \sigma QI$, where σ is molecular absorption cross-section (the probability that illumination photon will be absorbed by fluorescent dye), Q is fluorophore quantum yield, and I is the intensity of excitation light. The event that adversely affects the fluorescence is photobleaching, an irreversible phenomenon caused by illuminating photons' damage. A fluorescent molecule can only generate a finite number of photons which limits the time sample can be imaged [25].

For confocal fluorescence imaging, the excitation light is reflected by a dichroic mirror and directed to the objective lens, which focuses the incident beam as a spot on the specimen's focal plane. Fluorescence from the sample returns via the objective lens, and the longer wavelength light from the sample passes through the dichroic mirror to the detector. In front of the detector is a confocal aperture (pinhole) which allows only in-focus light to pass [25].

Differential interference contrast mode

Differential interference contrast (DIC), developed by Georges Nomarski, is commonly employed in a confocal laser scanning microscope. DIC is used to retrieve phase information from the phase objects in biology and observe topography in material science. It is especially suitable for a colourless, nearly transparent objects like tissue sections. This method provides relatively good contrast without the artefacts common in the phase-contrast imaging mode (halo effect).

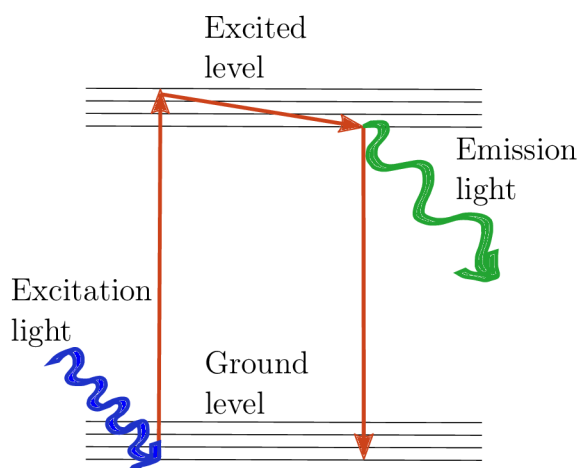


Figure 2.2: The energy level structure of a molecule, blue wave represents excitation wavelength and green emission wavelength.

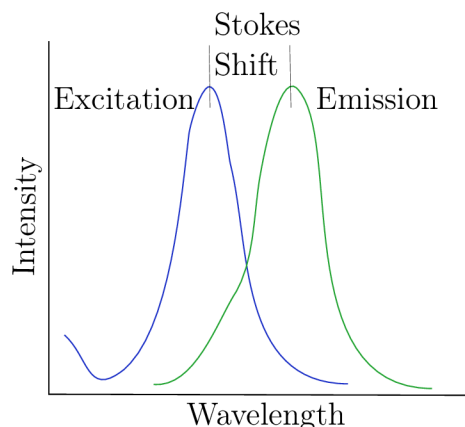


Figure 2.3: Diagram representing Stokes shift in wavelength between excitation and emission light.

The DIC principle is shown schematically in Figure 2.4 and can be described as follows. The light is plane-polarized by the polarizer so that its vibration plane is inclined by 45° to the plane of the diagram. The Wollaston prism is composed of two prisms glued together, made of birefringent (double-refracting) material. The optic axes of the two prisms are at right angles to each other. When the plane-polarized light hit the Wollaston prism perpendicularly, it will be split into two plane-polarized waves perpendicular to each other. The two beams can not interfere together because of the different polarization angle. The waves are deflected into two different directions at the border between the lower and upper prism (angular beam splitting): the first wave, the so-called ordinary wave, and the second wave, the extraordinary wave. Both waves have different refractive indices, and consequently, the ordinary wave has a higher speed than the extraordinary wave. The lateral separation of the two beams is only a few microns (smaller than the microscope's resolving power). The separation of two waves can be set by adjusting the crystal thickness [28, 29, 30].

As the two waves leave the prism, they have identical optical path lengths (optical path, $\Delta = nd$, where n is refractive index and d is a geometrical path). In the air, the two waves' speed is identical (they have the same refractive index). It is possible to introduce a path difference by simply shifting the Wollaston prism perpendicular to the direction of the incident light [28, 29, 30].

After passing through the condenser, waves go through the specimen, which causes an optical path difference between the two beams. This change is due to the variations in refractive index and geometrical thickness; one beam is affected more than the other [28, 29, 30].

In the second Wollaston prism, the two beams are recombined. In order to obtain interference of the two waves, their vibration planes must coincide. This is achieved by inserting the analyser into the path. After two beams enter the analyser, the light will get throughout at the single polarization angle - interference is now possible. The analyser is oriented to form 45° angle with the vibration plane of each of the entering

wave (this ensures both beams passing with the same intensity) [28, 29, 30].

This technique is susceptible to the changes in the curvature of specimen structure and refractive index gradients because of the small shear between the two waves. It shows increasing or decreasing phase gradients as differentially highlighted boundaries in the image. DIC can be implemented into a confocal microscope by simply inserting two Wollaston's prisms and analyser into the appropriate position [28, 29, 30].

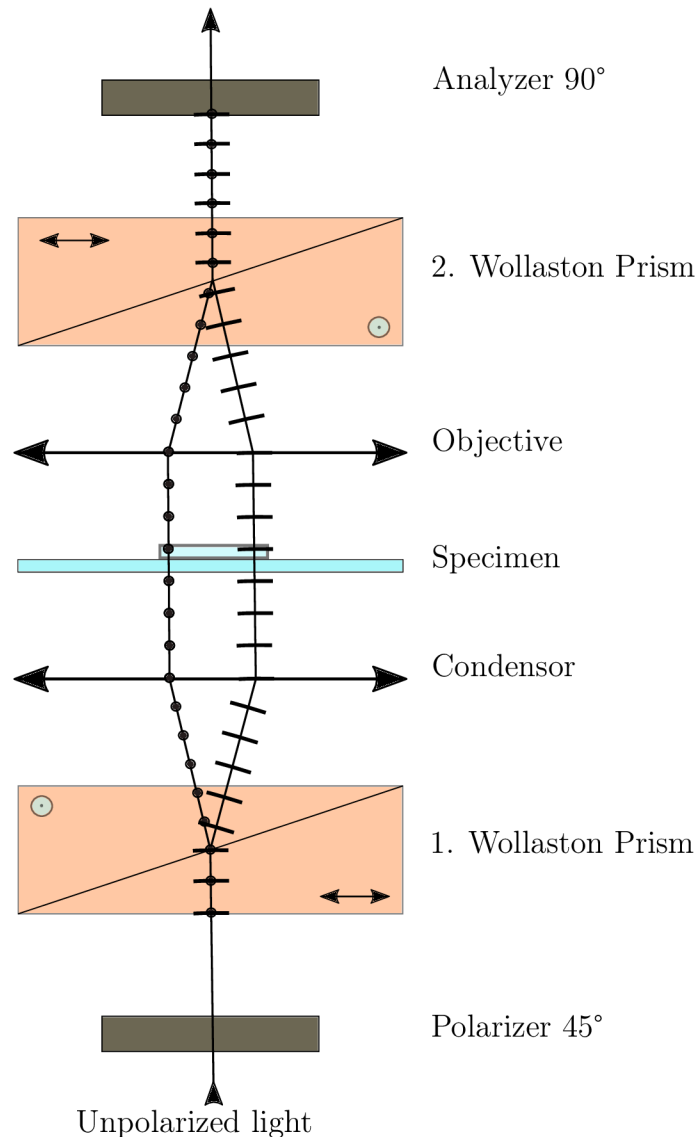


Figure 2.4: Scheme of DIC. Dotted line represents ordinary wave and comma line represents extraordinary wave [30].

2.1.2 Light Sheet Microscopy

Light Sheet Fluorescence Microscopy (LSFM) or simply "light sheet" (also referred as Selective Plane Illumination Microscopy (SPIM)) is a powerful tool especially for the biologists to achieve imaging of the whole specimens in 3D. With fluorescent proteins, different cell types can be imagined deep inside the tissue. The principle of this method

works on optical sectioning achieved by illuminating the sample with a sheet of light (few micrometers). SPIM has two optical paths, one for wide field detection and one for illumination with a thin sheet of light. Only the focal plane of the objective is illuminated, eliminating the risk of photobleaching. SPIM has been used to record fast-changing, weakly expressing tissues and to study the cellular and morphogenetic events in a real time within the entire embryo. The advantage over confocal microscopy is more efficient and faster optical sectioning, low photobleaching and ability of volumetric imaging [31]. Limitation of LSFM is requirement of optically transparent sample [32].

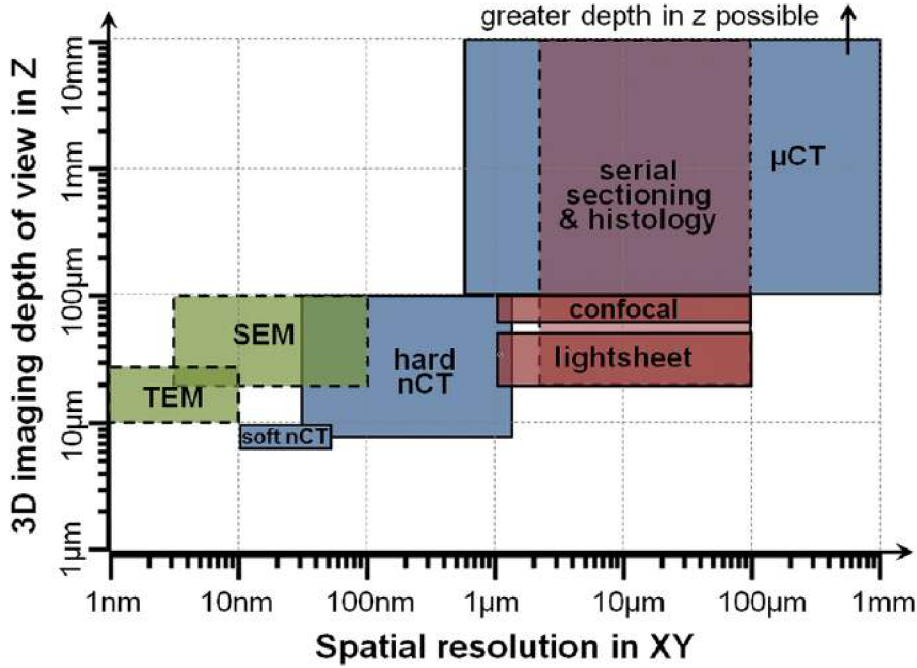


Figure 2.5: 3D imaging techniques for science application divided according to their spatial resolution (in XY) and the full depth of the volume that can be imagined (in Z). Blue - CT techniques (μ CT - micro computed tomography, nCT - nano computed tomography), green - electrone microscopy techniques (SEM - scanning electron microscopy, TEM - transmission electrone microscopy), red - light microscopy techniques (confocal and lightsheet). Techniques lined with dashed line are considered destructive. The picture is taken from: [32].

2.2 3D imaging with CT

In computed tomography (CT), the X-ray radiation is attenuated as it penetrates the objects. Therefore, different attenuation of the X-ray beam is producing absorption contrast. Beer-Lambert law (described in Chapter 1.4) can explain the exponential intensity loss of the beam. The equation can be rewritten in terms of the mass attenuation coefficient (μ/ρ) and show that the amount of attenuation is the number of atoms encountered by the X-ray beam.

$$I_t = I_0 \cdot \exp[-\mu/\rho \cdot \rho \cdot x] \quad (2.3)$$

I_t and I_0 are the intensities of the transmitted and incident X-rays, respectively. μ/ρ is mass attenuation coefficient, μ is linear attenuation coefficient and ρ is density of the material with thickness x . Mass attenuation coefficient is a function of the atomic number (Z) and wavelength (λ) of the photon ($\mu/\rho \sim Z^4\lambda^3$). There are other methods to evaluate the absorption coefficient but in the most models atomic number is mostly considered. The objects with higher densities and mass attenuation coefficient absorb additional X-rays [17, 33, 34].

μ CT imaging in biology is very similar to medical CT. One of the differences is that the sample (rather than the detector) is rotated, and projection images are taken for different angle orientation. The measurement can also take a longer time [10].

The limitation for cardiovascular tissue imaging is that contrast depends on the density and composition of the tissue. For imagining bone tissue, no contrast agents are needed since hydroxyapatite is dense enough to be detected. Various X-ray absorbing contrast agents (with high-atomic number elements) are being used to enhance the absorption contrast regarding soft tissue detection.

2.2.1 Contrast enhancing in soft tissue

Soaking the tissue in solutions with the high Z -elements increases the electron density of the tissue and thus the interaction with the X-rays increases. Therefore, the difference between tissue and background increases [35]. During the past few years, many different staining protocols have been developed based mainly on the pioneering work of Bryan D. Metcher. Other animal tissues have been scanned so far including whole murine embryos [36], murine brain [37, 8], nasal capsule [38] and hearts [39]. The most commonly used contrast stains are phosphotungstic acid (PTA) and inorganic iodine (I_2), which are less toxic than osmium tetroxide (OsO_4). PTA is a large molecule with tungsten ions, and hence it requires longer staining time to penetrate deep into the structure. PTA has trouble penetrating samples more than about 2 *mm* of tissue. Bryan D. Metcher suggested leaving samples in PTA for 2 hours to overnight or even longer. Staining time is not critical with this substance; PTA does not overstain [10]. Different scientists suggest different staining times with PTA. For the whole mouse embryo E15.5, the time from 7 to 12 days in 0.7% PTA was presented, depending on the type of mouse bred [40]. Descamps et al. proposed six days immersion in 2.5% PTA for E15.5 embryos [36] and Tesařová et al. suggested to place the whole mouse embryos in 0.7% PTA for six days [38]. Inorganic iodine (I_2) staining is easy to prepare. Tissue penetration is fast, but on the other hand, it may overstain some mineralised tissue. Therefore specific staining depending on the size and type of the sample should be considered [41, 40]. To avoid structural damage of soft tissue, a slow graded ethanol or methanol dehydration series were introduced to the standard protocols and final graded dehydration series at the end of the staining process. With these modifications, the authors reached excellent results [38, 42]. Even though many studies have been published regarding the contrast agents, little is known about their binding affinities towards a different tissue type [36]. Some claim that the staining methods are neither species-specific nor tissue-specific [41].

2.3 Imaging in phase-contrast

Detected intensity is modulated not only by absorption of the sample but also by a change of phase of X-ray waves travelling through the specimen. Phase-contrast imaging is suitable for samples (phase objects) that are composed of light elements, especially biological tissues, and does not require the usage of contrast agents. Explanation of this lies in the description of complex refractive index, which is written as [20]:

$$n = 1 - \delta + i\beta \quad (2.4)$$

The phase shift of X-rays passing through a specimen depends on the refractive index decrement δ , whereas absorbance β is related to a reduction in X-ray intensity. In other words, the decrement of δ means the phase shift, while the decrement of β means the absorption. Real part δ and imaginary part β are given by formulas,

$$\delta(\lambda) = \rho \frac{r_e \lambda^2 N_A Z}{2\pi A} \quad (2.5)$$

$$\beta(\lambda) = \mu(\lambda) \frac{\lambda}{4\pi} \quad (2.6)$$

where λ is the X-ray wavelength, ρ is the density of sample material, μ is the linear absorption coefficient, r_e is classical electron radius, N_A is Avogadro's number, Z and A are the serial number and atomic weight of the material, respectively. δ value for a soft tissue typically exceeds β . An estimation of δ and β values for soft tissue showed that δ is in range of $10^{-6} - 10^{-8}$ and β is in range $10^{-9} - 10^{-11}$ for 10 - 150 keV X-rays. Therefore, the differences in linear absorption coefficients are negligible in comparison with differences in phase shifts. Phase-contrast imaging is very sensitive for studying small variations of the analysed object. [20, 43]

This technique is widely used at the synchrotron, but with further development of X-ray sources and detectors, it is possible to use this method also in laboratory CT systems [12].

2.3.1 Phase-contrast imaging methods

There are different techniques used for phase-contrast imaging, and they are still evolving [20].

Crystal Interferometer Method

The first attempt to perform a phase-contrast image was made using LLL (Laue - Laue - Laue configuration) interferometer. The simple principle of this interferometer is shown in Figure 2.6. This interferometer has three plates made from a silicon crystal placed with identical gaps between themselves. The incoming X-ray beam is divided into two phase-coherent beams after passing through the beam splitter S and successively diffract from the second element mirror M . Beams converge together at the analyser A and form a standing wave. In practice, there usually appear some unwanted interference

patterns arising from strain and defects in the crystal. After placing the sample before the analyser, the intensity $I(x,y)$ of the interference pattern can be described by the formula:

$$I(x,y) = a(x,y) + b(x,y)\cos[\phi(x,y) + \Delta(x,y)] \quad (2.7)$$

where $a(x,y)$ and $b(x,y)$ are, respectively, the averaged background intensity and the interference pattern intensity, $\phi(x,y)$ is information about the phase, $\Delta(x,y)$ is the phase shift introduced by imperfections of interferometer, x and y are coordinates of the image [20, 43].

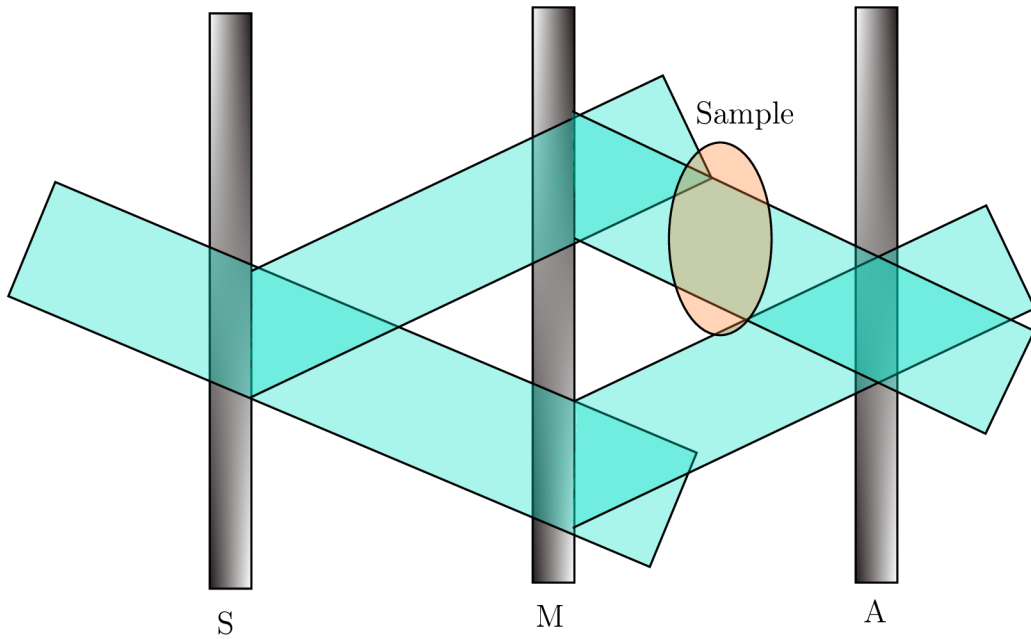


Figure 2.6: Crystal Interferometer method according to [20].

Talbot Interferometer Method

With a coherent wave passing through a diffraction grating, it is possible to observe the periodically repeated interference image of grating at Talbot distance:

$$d_T = 2mp^2/\lambda \quad (2.8)$$

where p is a grating period, λ is a wavelength, $m = 1,2,3,\dots$ and reconstruct the image of the observed sample. This is a phenomenon that was introduced in 1836 by Talbot. Afterwards, the fractional Talbot effect was discovered: a self-image of phase grating observed at a distance:

$$d_m = mp^2/2\eta^2\lambda \quad (2.9)$$

where the η is a coefficient equal to 1 if amplitude grating or a phase grating is with a phase shift of $\pi/2$; if $\eta = 2$ phase shift is π [43].

The Talbot interferometer (TI) method does not differ much from Crystal Interferometer (CI) Method. It is one of the methods based on *grating interferometry*. The schematic sketch of TI is shown in Figure 2.7. It is composed of two gratings G1 and G2. The role of the first (phase) grating G1 is to modulate periodic wave, similar to a standing wave introduced by the splitter S and mirror M in the CI method. Phase gratings are made from materials with low X-ray absorption. The interference pattern is much smaller than a pixel size at the detector. Therefore the second (absorption) grating G2 is used, so only part of the interference pattern passes through the slits onto the detector. The sample is placed before G1 grating and is deflecting the X-ray beam from the trajectory by the angle α . For the hard X-rays, the angle α is very small (few microradians) [20, 43] .

The interference pattern contains information about the phase shift and the X-ray absorption in the sample. The images of the sample are reconstructed by comparing the phase-shift recorded without and with the sample. For conventional X-ray tubes, it is necessary to place absorption G0 grating in front of the source to form a phase-contrast image with better contrast (Talbot-Lau interferometer). The critical condition for phase technique is imaging with coherent waves, so a small focal spot is needed. Unfortunately, laboratory X-ray sources exhibit a larger focal spot. Therefore, grating G0 is used, which function as a long array of micrometer-sized slits. Later, these three grating setups enabled the development of *dark-field or scattering (imaging)*. One of the difficulties in using the TI method is to fabricate analyser absorption grating G2 (necessary to introduce gold in it). There are also other new methods with different materials to prepare such gratings. With the development of high-resolution detectors, which can easily record a Talbot interference pattern, using G0 grating is not necessary anymore. [18, 20, 43]

According to Maier et al. TI method is the most promising phase setup for medical imaging [18].

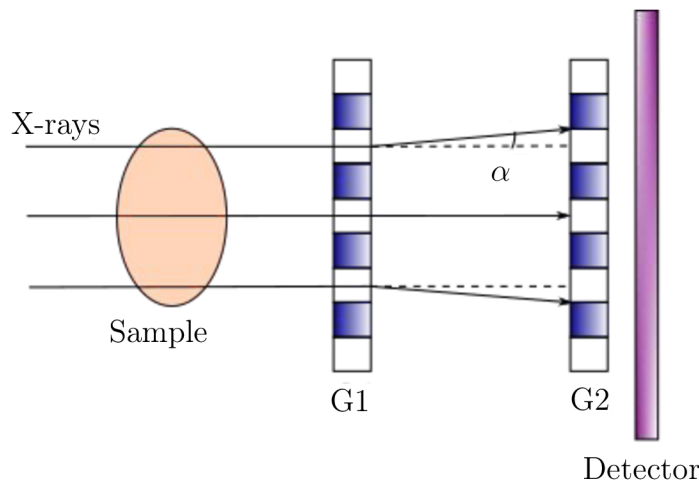


Figure 2.7: Talbot Interferometer method using principle of gratings according to [43].

Diffraction Enhanced Imaging

Diffraction-enhanced X-ray imaging (DEI) sometimes called *analyser based imaging* is sensitive to angular X-ray deviation (similar to TI). This method uses two crystals with a sample placed between them. The first crystal (monochromator) is used to produce monochromatic X-rays and to collimate the X-ray beam. Monochromatic radiation enables precisely to measure the refractive angle. The second crystal (analyser) is used as an angular filter; it reflects radiation only at the Bragg angle (very narrow angular interval). The rays which are not passing through the sample are not refracted. The ones interfering with the specimen are refracted, and the intensity at the detector is modulated by the change of angle incident on the analyser. This setup is shown in Figure 2.8 with a closer scheme describing the formation of phase-contrast in Figure 2.9. The advantage of exact measurements can be overshadowed by the need for monochromatic radiation and sensitivity to vibrations [18, 20, 43].

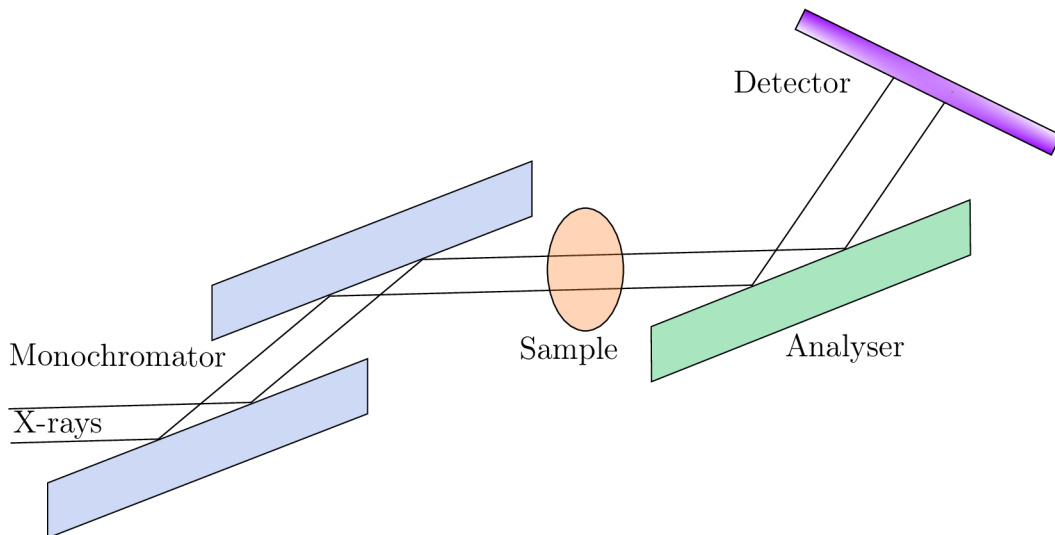


Figure 2.8: Optical scheme of DEI according to [43].

In Line Method

This method (also referred to as *Free-space propagation method* or *propagation phase contrast (PPC)*) is based on linear holographic effect: a phase shift introduced by a sample placed in the path of the coherent X-ray beam can be found at some distance due to Fresnel diffraction. It is the most frequently used approach in X-ray computed tomography imaging. According to Maier et al., it is the most straightforward phase-sensitive technique. Therefore, it is commonly used in laboratory CT systems [18]. Conditions estimating the X-ray phase contrast are for example focal spot size, wavelength or pixel size. For a larger source (focal spot size, $s = 100 \mu\text{m}$), the great image contrast is obtained for a small sample-detector distance R_2 . Considering smaller source diameter ($s = 50 \mu\text{m}$), increasing R_2 we can get more pronounced edge enhance-

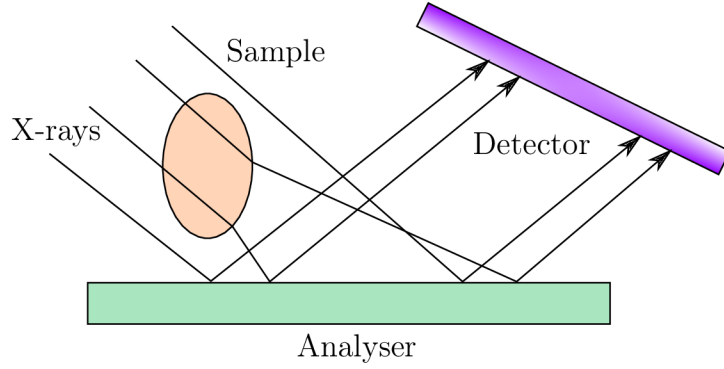


Figure 2.9: Scheme closely explaining the formation of phase-contrast image in DEI according to [43].

ment and the image had higher degree of contrast [44]. But the conditions, which are easy to set up, are:

- **imaging regime** (sample to detector distance - R_2)
- **coherence of X-ray beam**
- **geometrical sharpness**

The imaging regime can be quantified via Fresnel number N_F .

$$N_F = a^2/(\lambda z_{eff}) \quad (2.10)$$

where a is the size of the sample, λ is wavelength, z_{eff} is effective propagation distance defined as follows, $z_{eff} = R_1 \times R_2/R_1 + R_2$, where R_1 is source-sample distance and R_2 is sample-detector distance. Figure 2.10 describes the above mentioned geometric arrangement [12, 20, 43].

For $N_F \gg 1$ a purely absorption image can be observed at a small distance from the sample. $N_F \geq 1$ applies for an intermediate distance where can be observed Fresnel diffraction (near-field diffraction accompanied by interference intensity oscillations at the edges of the sample image, so-called edge effect). When $N_F \ll 1$, Fraunhofer (far-field or holographic) diffraction is observed, the actual structure is no longer recognisable due to the multiple fringes. To get visible structures in the image, near-field ($N_F > 1$) regime has to be maintained [20, 43].

Propagation based imaging needs a high degree of coherence of X-ray source which depends mainly on the focal spot size (considering X-ray source with finite focal spot size). Coherence can be evaluated by the ratio of shearing and lateral coherence length L_{shear}/L_{lat} . The source is almost fully coherent if the following condition is fulfilled:

$$\frac{L_{shear}}{L_{lat}} = \frac{s \times R_2}{a(R_1 + R_2)} < 1 \quad (2.11)$$

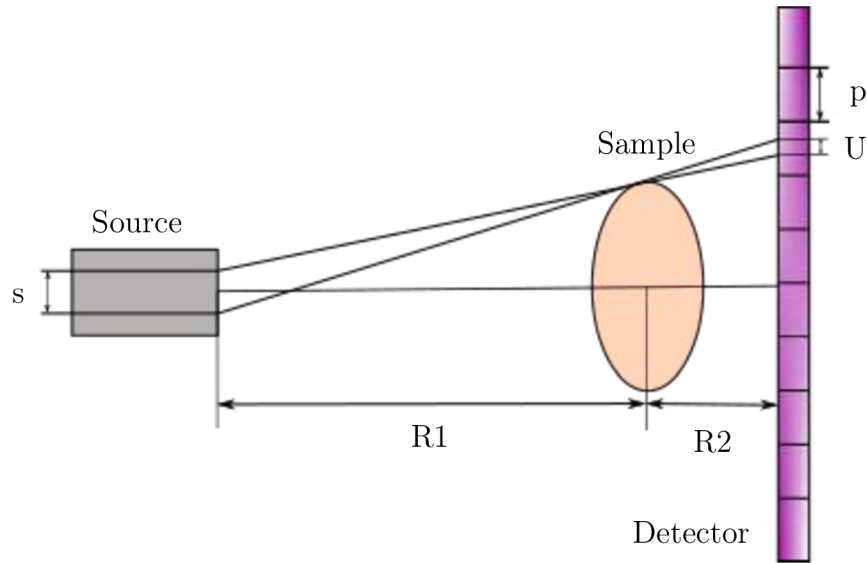


Figure 2.10: Geometric arrangement of propagation based imaging according to [12] where R_1 is source-sample distance and R_2 is sample-detector distance, s is focal spot size, U is geometrical unsharpness and p is pixel size.

where s is focal spot size, a is the size of the sample, R_1 is source-sample distance and R_2 is sample-detector distance [12].

Proper geometrical arrangements are needed to obtain a sharp image. The resolution depends on the focal spot size s as shown in Figure 2.10. The selected distances between source - sample (R_1) and sample - detector (R_2) effect the sharpness of the image (to obtain sharp image, pixel p has to be bigger than unsharpness U , $U < p$). Based on the geometry of the system, this means:

$$\frac{R_2}{R_1} \times s < p \quad (2.12)$$

For the laboratory cone-beam X-ray sources geometrical unsharpness must be considered [12].

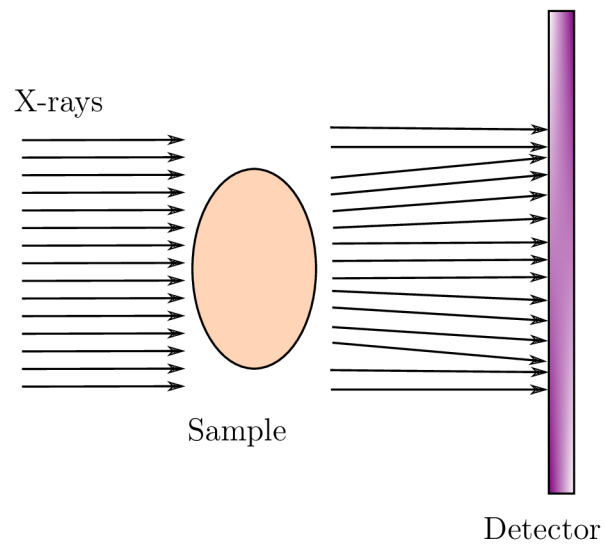


Figure 2.11: Scheme closely explaining the formation of phase-contrast image in PPC according to [43]

3. Experimental part

Master's Thesis goals:

- suggestion of the method for a computed tomography measurement
 - selection of the best staining agent for a mouse embryonic heart
 - performing the measurement of selected samples on μ CT
 - reaching the high-micron resolution
 - application of a phase-contrast imaging
- proposal of the analysis of the obtained data
 - segmentation of anatomical parts
 - application of available software tools for evaluation

3.1 Introduction

Thanks to genetic engineering of mouse genome, scientist are able to identify many genes which are essential for embryogenesis. Laboratory mouse models remain the superior model to describe early defects during development. Up to one-third of different mutations are nonviable thus it is not possible to experiment on adult mouse [45]. Genetically modified mouse models with abnormalities in cardiovascular system help to understand mechanisms that regulate human heart development and to discover the cause of congenital defects. According to Degenhardt et al., cardiac defects are the most common serious anomalies among new born babies [1]. The aim of my work was to analyse mouse embryonic heart E17.5 (17.5 days post fertilisation).

Conventional histological methods are based on cutting tissue into thin slices and after that imagined using a microscope. However, they are labour-intensive and time-consuming. Moreover, they can introduce tissue stress or induce artefacts to the samples, allowing evaluating information only from a limited amount of 2D sections. In the third dimension, a resolution is limited to section thickness. It is important to realise that some material might be lost due to a preparation technique. [46]. On the other hand, histological examination achieves a sub-micrometer resolution of the microanatomy, i.e. microstructures and morphology [47]. Studies related to mouse embryonic hearts and its possible defects could benefit from novel technique allowing fast and precise inspection of whole heart structure. High resolution contrast-enhanced μ CT allows

fast non-destructive 3D visualisation and quantification [47]. Contrast agents helped to enhance the absorption contrast and the soft tissue was imaged with resolution $2.3 \mu\text{m}$ voxel size.

3.2 Materials and Methods

3.2.1 Sample preparation

In order to prepare biological samples for different imaging techniques, the pregnant mouse was sacrificed. After excision, the embryos (E17.5) were fixed in 4% paraformaldehyde. For embryos E17.5, it is beneficial to make an incision under the heart for better solution penetration. Samples were stored in $+4^\circ\text{C}$ in mild rotation until further use.

3.2.2 Histological samples

To prepare samples for cryosections, the heart was dissected from embryos, washed few times in PBS (Phosphate Buffered Saline), and placed in 30% sucrose for a short amount of time before embedding in O.C.T. (compound, based on water-soluble glycols and resins, used to quickly embed fresh tissue specimens for frozen sections using a cryostat) [48]. Samples are stored at -20°C or -80°C and later sectioned using a cryostat machine into $14 \mu\text{m}$ thick slices. To minimise tissue loss, sections are placed on adhesion glass slides. The slides were submerged in antigen retrieval solution (to improve the immunohistochemistry response by increasing the accessibility of antibodies to tissue antigens) [49]. The slides were washed in PBST (Phosphate-Buffered Saline, 0.1% Tween), and the fluorescent DNA stain (DAPI) was used. In this step, the other types of antibodies can be added if necessary. After the incubation period, slides were washed in PBST and mounted with 70% glycerol to be visualised with a confocal microscope.

Different mouse heart sections in various planes were imaged using an inverted confocal microscope: Zeiss LSM 880, objective: C-Apochromat 40x/1.2 W Corr FCS M27. For a more informative visualisation of biological tissue, two channels were used. First, using fluorescence contrast mode to imagine the cardiomyocyte's nucleus. The second, the brightfield contrast method with differential interference contrast, visualises the structure, size, and orientation of individual muscle fibres in the heart. The principle of both methods is described more in detail in Chapter 2.1.1. The excitation wavelength was 405 nm , and the emission wavelength was 471 nm . The pinhole during the imaging has been set to 7.62 AU (Airy Units = diameter of the first minimum of the Airy disk), which corresponds to $131 \mu\text{m}$. Three slices in the z direction have been taken, covering the range in depth $2.97 \mu\text{m}$. Figure 3.1 shows channels: fluorescence, brightfield and merged channel and Figure 3.2 zoomed in detail visualising three slices in the z direction.

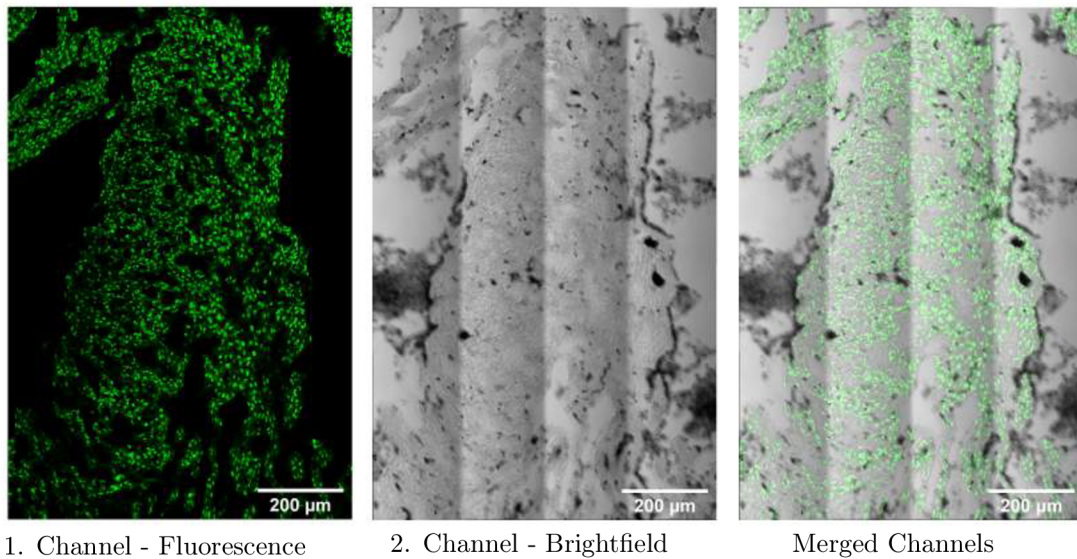


Figure 3.1: Images of the interventricular septum from a confocal microscope. Images from left to right: 1. Fluorescence channel with green-labelled nucleus with DAPI, 2. Brightfield channel using DIC principle to image tissue structure, 3. both channels merged.

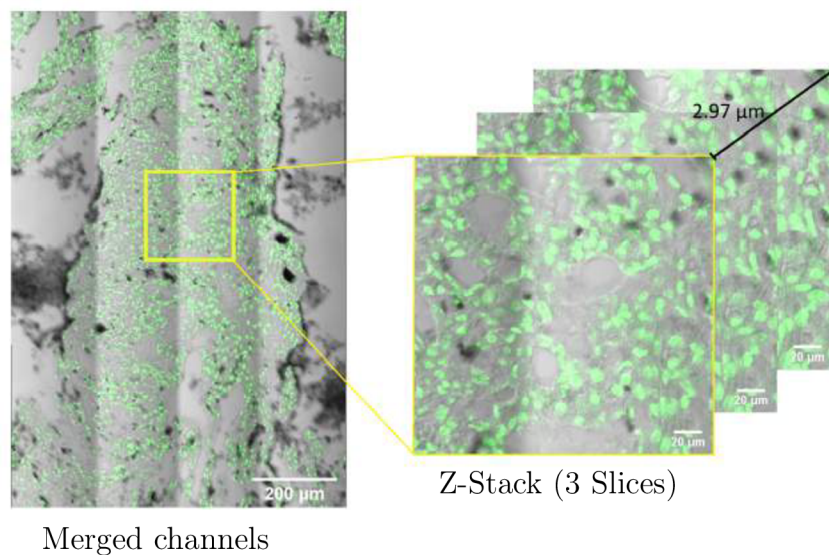


Figure 3.2: Images of the interventricular septum from a confocal microscope. Both channels merged, detailed Z-stack of 3 slices.

3.2.3 Samples for Computed Tomography

Samples were washed in PBS (Phosphate Buffered Saline) and dehydrated in methanol gradient (30%, 50%, 80%, 90%). For the staining protocols, the samples were divided into two categories. In the first category, samples were stained as whole embryos, whereas in the second group, the heart was excised and stained as a separated organ. Various staining reagents (Table 3.1) and different staining times (Table 3.2) were used. The rehydration process followed after the individual staining procedures were done. Samples stained with PTA and with I_2 were rehydrated in methanol gradient (90%, 80%, 50%, 30%) and (60%, 30%), respectively, each concentration for two days. After that, mouse hearts were transferred to PBS.



Figure 3.3: Example of one sample before staining.

| Contrasting agents | |
|--------------------|----------------------------|
| PTA | 1% (w/v) PTA in 90% MeOH |
| I_2 | 1% (w/v) I_2 in 90% MeOH |

Table 3.1: Chemicals used for staining mouse hearts.

Generally, the higher concentration of contrasting agent means faster penetration to the tissue but, on the other hand, may introduce a higher degree of tissue shrinkage [50]. Contrast agents were dissolved in alcohol with lower X-ray attenuation than water; thus, discrimination between tissue and background is better [51].

After the results were analysed (Chapter 3.3.1), I decided to optimise staining protocols to reach an even better outcome. For this time, only separate mouse heart samples were used. Dehydration in ethanol gradient (30%, 50%, 70%, 80%, 90%) - 30 min in each concentration was followed by the staining, for one sample in I_2 , and the other in PTA. After staining, a rehydration process in ethanol gradient was performed (5 min in 50%, 15 min in 30%).

Before the μ CT measurement, the samples were embedded in 1% agarose gel and placed in a plastic tube to stabilise during scanning. The plastic tube was fixed with

| Mouse embryo E17.5 | Staining time and substances |
|--------------------|----------------------------------|
| N.1 (Whole Embryo) | 3 weeks in PTA |
| N.2 (Whole Embryo) | 2 weeks in PTA + 2 days in I_2 |
| N.3 (Heart) | 10 days in PTA |
| N.4 (Heart) | 6 days in PTA + 1 day in I_2 |
| N.5 (Heart) | 24 hours in I_2 |

Table 3.2: 1. experiment - preparation of the samples.

| Mouse embryo E17.5 | Staining time and substances |
|--------------------|------------------------------|
| N.6 (Heart) | 3 hours in I_2 |
| N.7 (Heart) | 2 hours in PTA |

Table 3.3: 2. experiment - preparation of the samples

glue to the metal rod. Then it was mounted in the chuck inside of the micro CT cabinet to provide a stable position.

3.2.4 Measurements with μ CT

Before the measurement, X-ray images were taken to check if the tissue is stained enough (Figures 3.5 and 3.6). In this step, the decision to discard sample N.5 (24 hours in I_2) was made. From the Figure 3.6 it is discernible that the contrast is not sufficient.

The samples were imaged using GE phoenix v|tome|x L240 system in an air - conditioned cabinet. The system is equipped with two X-ray tubes which can be chosen according to the sample size. The microfocus tube is designed to reach voltages up to 240 kV and the nanofocus tube up to 180 kV. The first tube can achieve more flux, thus investigate large samples. The settings were set based on the long-term experience of CEITEC BUT Brno μ CT research group and are explained more in detail in Tesarova's diploma thesis along with recommended tube settings for different materials from GE phoenix v|tome|x L240 producer [52]. The same parameters were used on E15.5 days old stained embryos while achieving excellent results. The group was investigating craniofacial cartilage development in mouse embryos [38].

The data was acquired using a flat panel detector DXR250 with 2048×2048 pixels, $200 \times 200 \mu m^2$ pixel size. The system used acceleration voltage 60 kV and tube current $200 \mu A$. Binning was set to number 2 to improve signal-to-noise and to reduce the size of image data. The beam was filtered by 0.2 mm thick aluminium filter. Exposure time was determined to 500 ms, and three images were averaged for reducing the noise. The total scan time was 1:25 hour. 2400 projections were taken over 360° . The voxel size of the obtained volume was $2.3 \mu m$. The tomographic reconstruction was done using the GE phoenix datos|x 2.0 software (GE Sensing & Inspection Technologies GmbH, Germany). Reconstructed images were exported as vgl formats and further processed in VGStudio MAX 3.4.

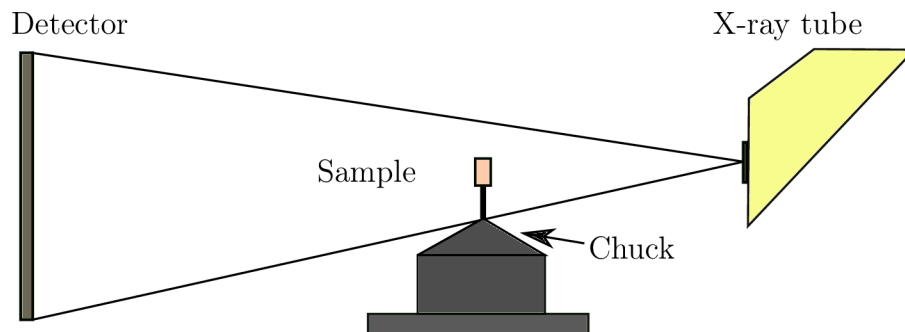


Figure 3.4: A schematic drawing of industrial μ CT with flat panel detector, x-ray tube with aluminium filter, sample embedded in agarose gel in the tube and mounted in the chuck.

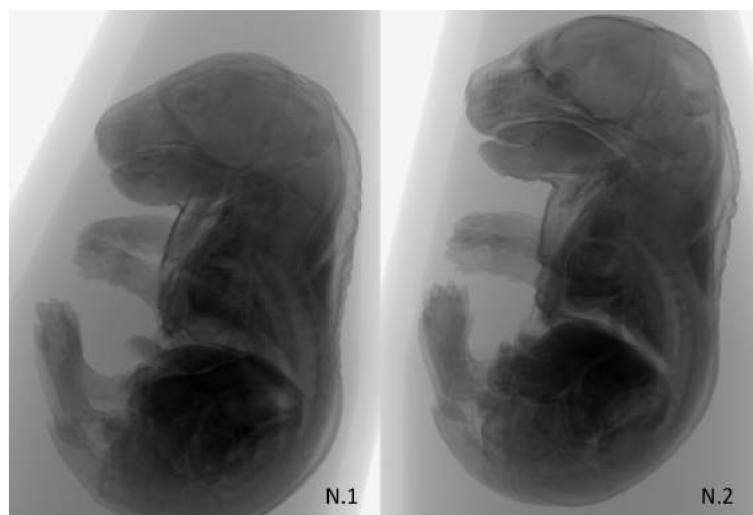


Figure 3.5: X-ray pictures of contrast-enhanced mouse embryos (N.1 and N.2, stained according to Table 3.2) to see the quality of stained soft tissue before scanning with μ CT.

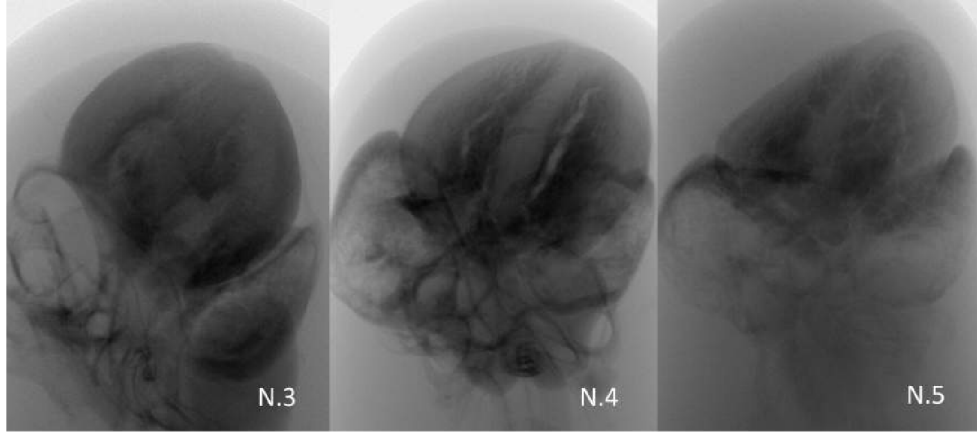


Figure 3.6: X-ray pictures of contrast-enhanced mouse hearts (N.3, N.4 and N.5, stained according to Table 3.2) to see the quality of stained soft tissue before scanning with μ CT.

3.3 Results

3.3.1 Image quality evaluation

Different parameters can characterise image quality (contrast, noise, image sharpness). Various influences might appear during scanning, affecting image quality (hardware and user-set scan parameters, software-related effects such as reconstruction artefacts and filtering) [53].

The CT scan's qualitative evaluation has been performed by plotting four normalised histograms of 4 samples in one graph and comparing their shape (Figure 3.7). A histogram is used to describe CT value distribution, where the x axis value represents the brightness of individual pixels. The y axis represents the number of pixels of specific brightness. For 16 bit image the grey value ranges from 0 (black) to 65 536 (white). The taller peak shows the pixels, which represents the background of the scanned specimen. The smaller peak is the material of interest - tissue. The histograms showing a more prominent saddle point and greater distance between 2 peaks represent better discrimination between background and tissue. Therefore, N.3 (10 days in PTA) is not fulfilling expectations of a good staining.

Another method to qualitative evaluate the CT scans is to calculate CNR (Contrast-to-Noise Ratio) and SNR (Signal-to-Noise Ratio). Noise, or standard deviation of the pixel grey value, is a random fluctuation of the signal. It is one of the most important parameters for evaluating image quality and is considered in CNR and SNR. If noise is too high, a specific grey value cannot be assigned to the background or object. One of the advantages of considering a standard deviation for the noise results in similar CNR values for different noise structures [53]. CNR is a parameter that enables detection of defects in volume. Low CNR leads to decreased detectability. It can be calculated using mean grey values of background μ_b , object μ_o and noise σ_b by the following equation:

$$CNR = (\mu_o - \mu_b) / \sigma_b \quad (3.1)$$

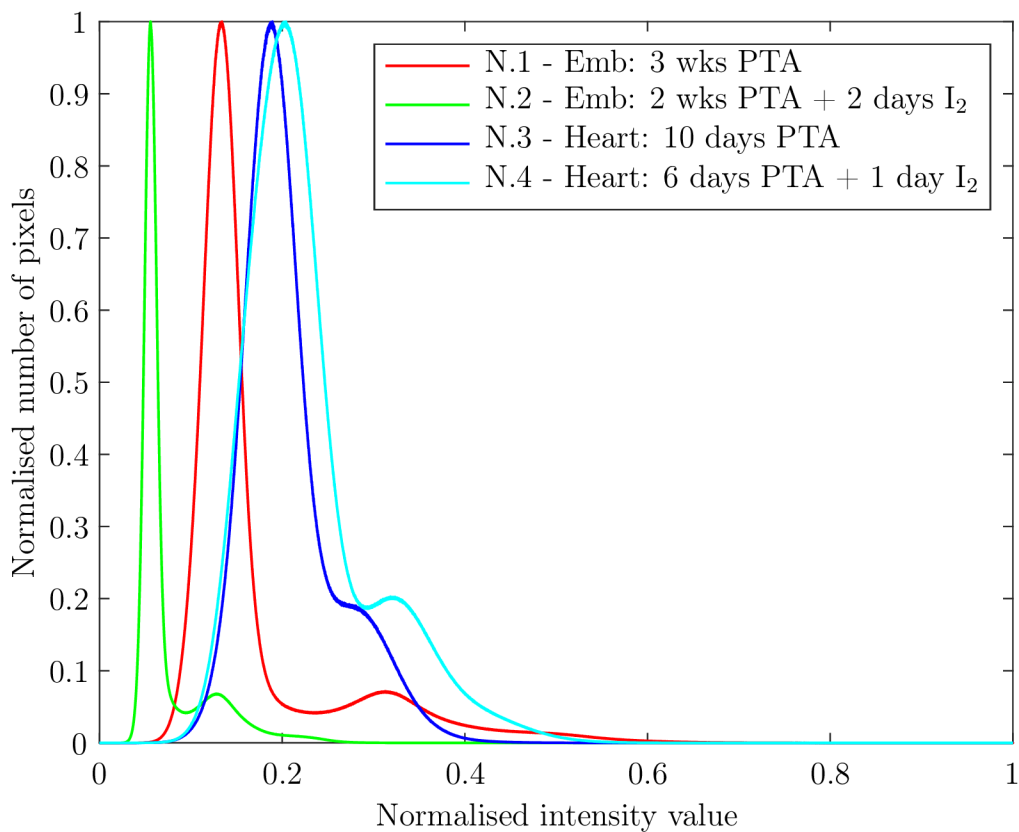


Figure 3.7: 1. experiment - Histograms of the grey value of 4 mouse hearts (E17.5) from μ CT data. The taller peak shows the pixels, representing the background of the scanned specimen. The smaller peak is the material of interest - tissue. The histograms showing a more prominent saddle point and longer distance between 2 peaks represent better discrimination between background and tissue. Peak distances correspond to the values in Table 3.4.

SNR is a merit for the detectability of an object in a noisy image. It is described as the ratio between the mean grey value of the object to the noise in the same region.

$$SNR = \mu_o / \sigma_o \quad (3.2)$$

Table 3.4 shows that the best values of CNR and SNR have the sample number 1. The number 2 represents good staining as well. In conclusion, the best staining protocol was shown in samples number 1 and 2, which means staining whole embryos in PTA for a longer time (2 to 3 weeks). There might be different reasons why other protocols were not considered sufficient. For instance, handling small organs is more difficult and prone to mishandling than the whole bodies. Therefore, the second experiment was suggested with a shorter time for the rehydration process. More days in methanol gradient might have caused washing away the contrast agents from separated hearts.

| #N | Peak distance | CNR | SNR |
|----|---------------|------|------|
| #1 | 11 706 | 13.5 | 13.9 |
| #2 | 4 723 | 12.9 | 11.0 |
| #3 | 5 754 | 3.0 | 11.1 |
| #4 | 7 501 | 2.7 | 9.1 |

Table 3.4: 1. experiment - Comparison of distances of two peaks, calculated values of CNR and SNR (CNR - Contrast-to-Noise Ratio, SNR - Signal-to-Noise-Ratio)

A new staining protocol was suggested to achieve better image quality (Table 3.3). Only separated mouse hearts (E17.5) were used, and most importantly, the time for rehydration was shorter, so the contrasting agent should not wash out. Moreover, the whole time of sample preparation has shortened.

| #N | Peak distance | CNR | SNR |
|----|---------------|------|------|
| #1 | 11 706 | 13.5 | 13.9 |
| #2 | 4 723 | 12.9 | 11.0 |
| #6 | 13 782 | 24.1 | 15.9 |
| #7 | 15 958 | 24.5 | 17.7 |

Table 3.5: 2. experiment - Comparison of distances of two peaks, calculated values of CNR and SNR (CNR - Contrast-to-Noise Ratio, SNR - Signal-to-Noise-Ratio) of the two best staining protocols from the 1. experiment (N.1 and N.2) with 2. experiment (N.6 and N.7)

In conclusion, the 2. experiment brought better results with more clear discrimination between background and tissue (more prominent saddle point in the histogram of grey value, Figure 3.8). They have less noise (values CNR and SNR are higher than in the 1. experiment, Table 3.5). The best staining protocol with higher CNR and SNR numbers is N.7: 12 hours in PTA. PTA has proven to be the best contrast-enhancing substance for small biological samples because it is more stable during dehydration and

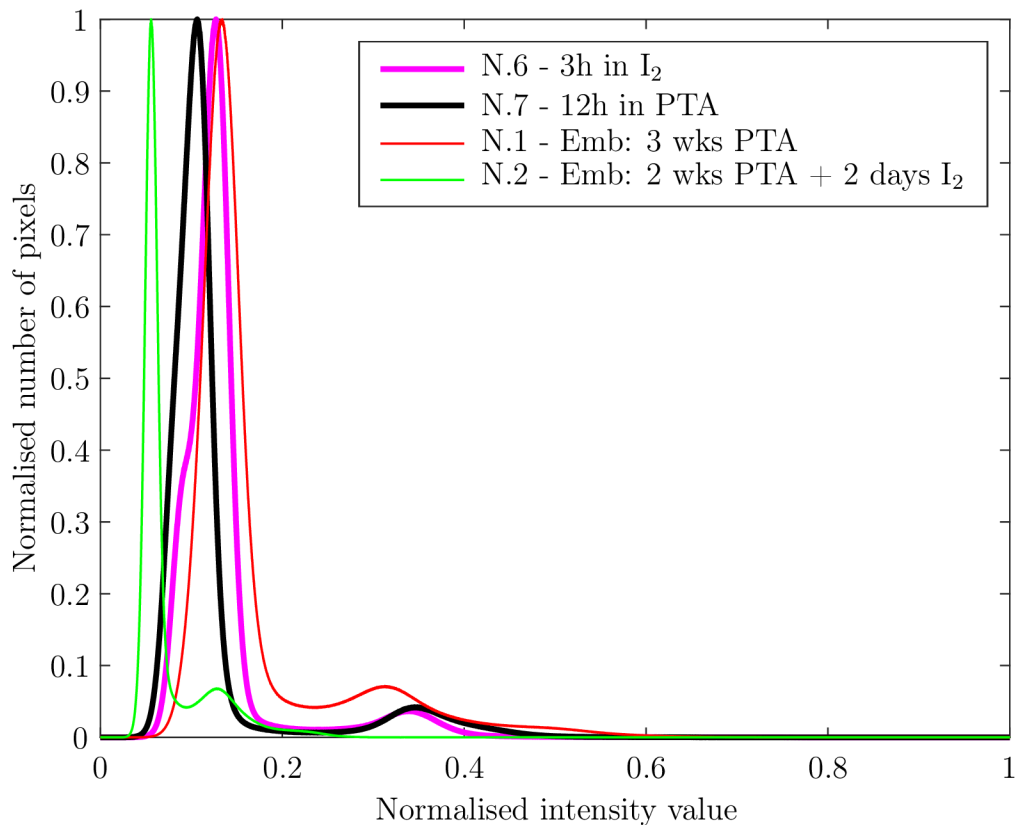


Figure 3.8: 2. experiment - Histograms of the grey value of 4 mouse hearts (N.1 and N.2 from the 1. experiment and N.6 and N.7 from 2. experiment) from μ CT data. The taller peak represents the background of the scanned specimen, and the smaller peak is the tissue. Histograms of N.6 and N.7 show a more prominent saddle point and longer distance between 2 peaks than original histograms. Peak distances correspond to the values in Table 3.5.

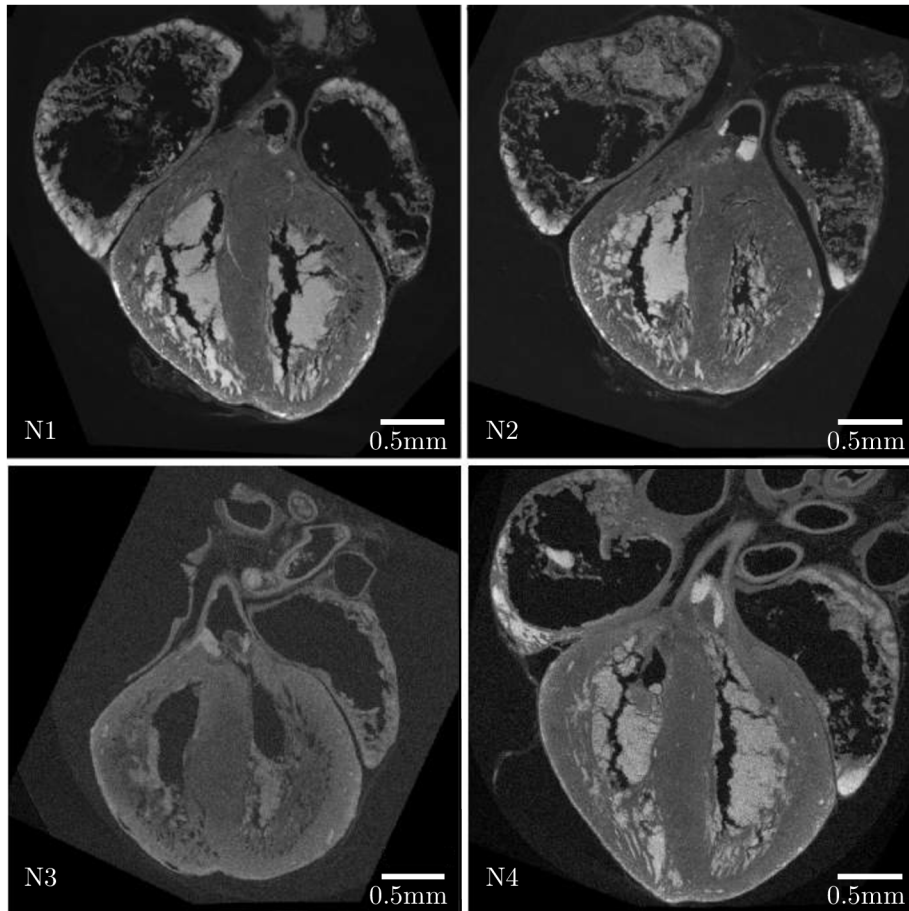


Figure 3.9: 1. experiment. One tomographic slice of stained mouse hearts E17.5 (N.1 - N.4), frontal plane

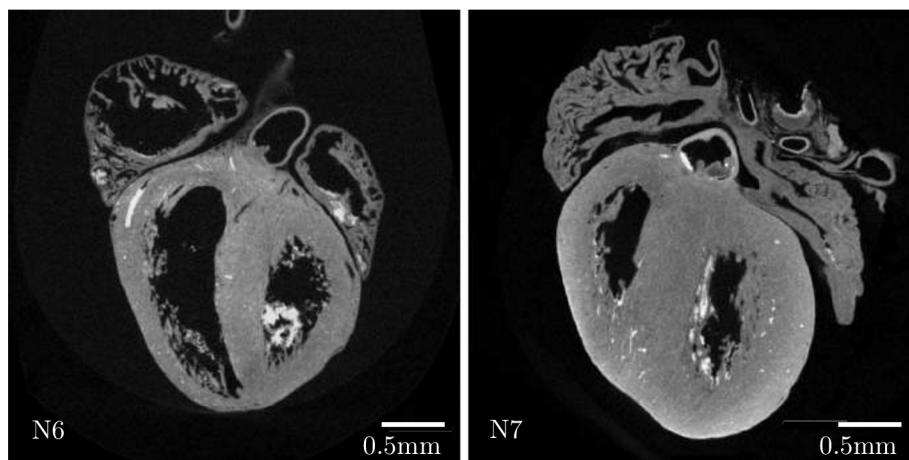


Figure 3.10: 2. experiment. One tomographic slice of stained mouse hearts E17.5 (N.6 - N.7), frontal plane

rehydration process. Moreover, it is less toxic than I_2 and does not overstain the tissue. On the other hand, it requires a longer staining time.

3.3.2 Processing of the data

Anatomy and physiology

Most of the experiments are carried out in mice considering 99% genetic homology between the two species: mouse and human. The murine animal models are widely used for the studies of defects considering the anatomical similarities between mammals. Most of the mouse mutations are not viable post-natally. Therefore, it is common to examine morphology in late gestation. Throughout the development, mouse and human embryos carry the same anatomical features. Especially the anatomy of the heart is very similar [54]. To segment the mouse heart properly, the study of murine heart anatomy and similarities with humans was unavoidable.

Both species' heart has four chambers divided into two atria and two ventricles, separated by the interventricular septum (IVS). The connection between atria and ventricles is provided by valves, tricuspid for the right part of the heart, and bicuspid (mitral) valve for the left part. Cardiovascular structures are referred to as right or left based on their contribution to the pulmonary and systemic blood circulation, respectively. Two main vessels are responsible for the blood flow between the heart and the lungs and the heart and the body. The aorta is the main artery in the body and is connected to the left ventricle, distributing oxygenated blood from the lung to the whole body. In contrast, the pulmonary artery is connected to the right ventricle and carries deoxygenated blood from the body to the lungs as a part of pulmonary circulation.

In this work, the main focus was to study four chambers of the heart: atria, ventricles and IVS. The walls of ventricles are thicker than atria's; thus, the myocardium's overall volume in ventricles is bigger. The inner part of the ventricles is lined with myocardial protrusions known as trabeculae (trabeculae carneae), while the heart's exterior walls are generally smooth. It is believed this lumen is created during development by hemodynamic forces (wall shear stress, blood pressure) [55]. Each atrium is composed of an appendage (the areas at the tips of atria, LAA - left atrial appendages, RAA - right atrial appendages), a venous component, and a muscular vestibule. The venous component of the left atrium is less prominent than in the right atrium. Two atria are separated by an interatrial septum (IAS). This structure is closed in the fully formed heart, but during development, it is an aperture termed as foramen ovale [54, 56].

Even though the heart's main parts are the same, it is crucial to point out some differences between mouse and human. Apart from the apparent difference in size, the most pronounced difference in external features is found in their overall shape. The human heart has a pyramidal shape, whereas the mouse heart has a more ellipsoidal shape. Another difference is that atria in the human heart are more prominent structures than in mouse [57]. The most significant variations in anatomy are probably in the venous pole of the heart. (The right atrium collects blood from the left and right

superior caval veins (LSCV and RSCV) and inferior vena cava (IVC)). LSCV regresses in healthy human heart, whereas in mouse it persists into postnatal life. The four pulmonary veins found in humans are in mice fused into a single collector that enters the left atrium [58]. A better description of differences between human and mouse heart can be found in the literature [57].

In the age E17.5, the heart has already achieved a definite prenatal configuration. Nevertheless, the embryonic blood cycle is distinct from the adult heart in these aspects (Figure 3.11): Oxygenated blood from the placenta flows through the IVC. IVC enters the right atrium (RA) and continues through the interatrial septum via foramen ovale to the left atrium (LA) and the left ventricle (LV). From there, the blood is pumped through the aorta to the body. Deoxygenated blood is entering RA through the right superior vena (RSV), continues to the right ventricle (RV) and from there to the pulmonary trunk (PT). From there, the blood is supposed to go to the lungs. Lungs are not yet functional, and the resistance is high; the majority of the blood is shunted through the ductus arteriosus into descending aorta (DA). After birth foramen ovale and ductus arteriosus are closed, and separate pulmonary and systemic circulation is formed [59].

The segmentation of separate anatomical structures was based mainly upon the following literature: [56].

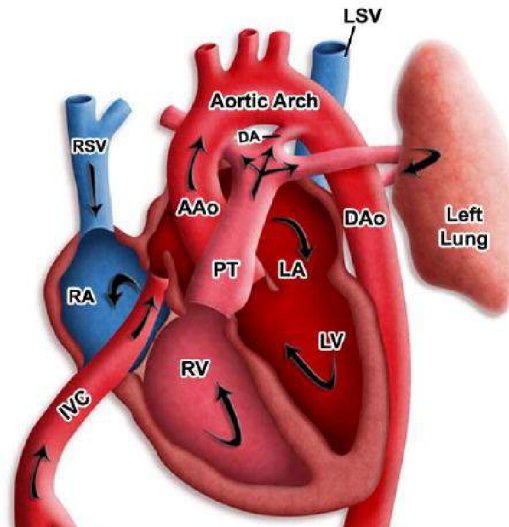


Figure 3.11: The blood flow in the prenatal mouse heart. Modified from: [59].

Segmentation

3D volume visualization, segmentation and volumetric analysis of the contrast-enhanced mouse heart (E17.5) were processed with Avizo 2020.2 segmentation software. After tomographic reconstruction we obtain series of 2D greyscale pictures. Reconstructed data were exported from VGStudio as a DICOM image stack and opened in Avizo.

Segmentation of digital image data means dividing the image into several disjoint regions to obtain a better analysis. Assigning labels to image voxels of soft tissue might be challenging. The mouse heart is a complex structure with the same value of contrast

for muscle; thus, at some point, manual segmentation is inevitable to precisely segment all anatomical parts.

The key is to use a specific combination of various segmentation tools available in Avizo. The first step was to separate the heart from the background using a watershed tool. It is one of the most common segmentation algorithms used in medical and material science images [60]. The watershed segmentation algorithm represents a greyscale image as a topographic relief where each voxel's intensity value (considering 3D image) represents its height. This relief consists of valleys (minimums), high-altitude ridges (watershed lines) and slopes (catchment basins). The principle of this segmentation method is to localise catchment basins and/or watershed lines since each catchment basin is considered as a separate part of the image. There are two main ways how to find watershed lines: by flooding and by rain falling. Avizo 2020.2 uses principle by flooding. In the beginning, the user has to define "seed points" = catchment basins. By defining these "seeds", the algorithm simulates flooding areas, gradually expanding until it reaches watershed lines. More details about watershed algorithm can be found in literature [60]. After defining "seed points," a gradient image is created, which will provide the landscape image controlling the markers' expansion.

Module arithmetic allows the user to perform calculations on data sets with user-defined expression. I used it to assign segmented material of heart to number 1 and multiplied this result with original greyscale data (Figure 3.12).

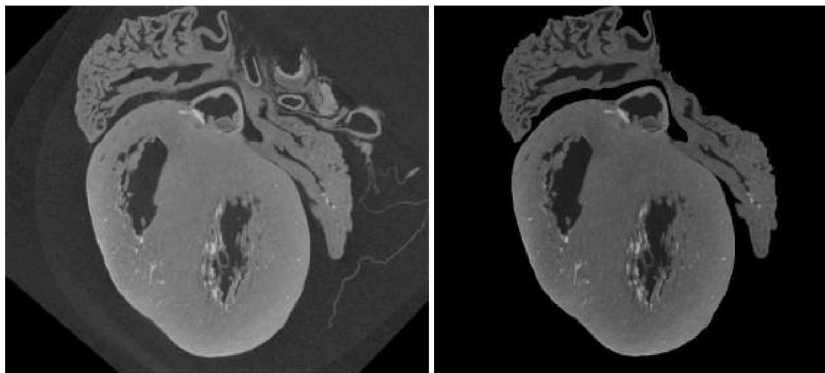


Figure 3.12: Separation the heart from the background. Left: original image. Right: result after watershed and arithmetic module.

Avizo provides a wide range of fully manual to purely automatic segmentation tools. Threshold segmentation requires less manual interaction but usually requires a higher image quality. The data were scanned with $2.3 \mu\text{m}$ voxel size, thus providing perfect data for thresholding. Segmentation is achieved based on grey values of the image data. Firstly, black voxels were separated and classified as background. Then, I manually set the range for pixel intensity for residual blood, which might occur in heart chambers (white voxels), myocardial muscle (grey voxels) and air in chambers (dark voxels). This process is fast and provides accurate discrimination between muscle, blood and air.

To separate right/left atria, ventricles and interventricular septum, manual segmentation is inevitable. I used lasso (contouring) and brush (painting) tool to segment the approximate area of atria, ventricles and septum (precise segmentation of the outer

boundaries is not necessary, this will be achieved in the next step). The Lasso tool draws a closed contour and selects all pixels within the contour. For interventricular septum segmentation, the brush with enabled masking was used. The masking feature lets the user control the masking by setting range (from 0 to 65 535) and its visibility in 2D or 3D viewer. This selection was made every 20 to 30 slice, and segmented areas were interpolated. Avizo will interpolate the empty slices based on the segmented slices' information, and the 3D segmented volume can be visualised.

In the last step, I multiplied each segmented area with muscle and air (segmented by thresholding) to get a precise area of the right/left atrium and ventricle muscle and the empty volume of each chamber. The blood was added to the air to represent the maximum volume of each heart chamber accurately.

Segmentation protocol of mouse heart has been achieved within 4-5 hours. Each anatomical part was saved as an STL (STereoLithography) file and loaded to VGStudio MAX 3.4 for further analysis.

3.3.3 Analysis of 3D models

VGStudio MAX 3.4 is the software for voxel data analysis and visualisation in industrial computed tomography with a vast range of applications. I loaded segmented meshes from Avizo one by one to VGStudio to improve the heart structure's visualisation and analysis (volumetric analysis, wall thickness analysis). VGStudio offers image processing operations, for instance, morphological operations like erosion (removes pixels on object boundaries) and dilatation (adds pixels to the boundaries of region of interest - ROI). The user can define the expansion or contraction of the ROI by a specified number of voxels. The other, but a similar method, is opening (erosion followed by dilatation) and closing (dilatation followed by erosion). These morphological operations are useful for eliminating small holes inside the ROI or eliminating small particles outside the ROI. Another method to improve image segmentation result is morphological refinement. Refinement adjusts the borders of the ROI using the local grey value gradients. The final tool used for the improvement of the borders of selected ROI is smoothing [61]. Using all the mentioned tools provided an important step in 3D image visualisation of segmented anatomical parts from Avizo.

Volumetric analysis

Embryonic heart development is a complicated and dynamic process, and the complete understanding of its complexity is still missing. During cardiogenesis, the size and shape of chambers vary greatly. μ CT has been previously used to study congenital defects where it provides the resolutions of structures that are too small to be measured by physical dissection and weighing [2, 62]. The volumetric measurement of chick embryonic hearts was previously performed, for example, by Butcher et al. [62]. Another study compared the volume of the left ventricle (LV) of adult mouse hearts from μ CT with LV dissected in the laboratory, proving that μ CT provides a non-destructive, efficient and accurate visualization tool for anatomical analysis of animal heart models of human cardiovascular conditions [2]. Mass of LV has shown to be linked with

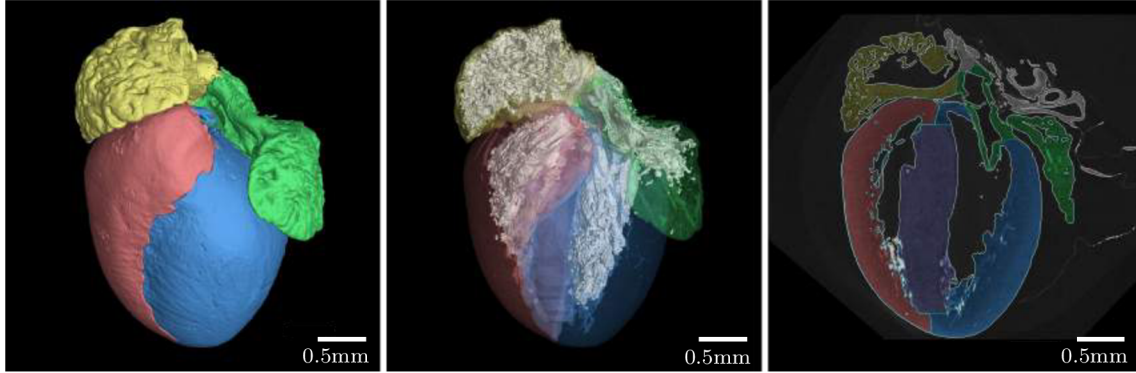


Figure 3.13: Pictures are showing four chambers of mouse heart (E17.5), right ventricle (red), right atrium (yellow), left ventricle (blue), left atrium (green), interventricular septum (purple). The middle image shows in white the inner cavity of each chamber. The picture at right is a frontal cut through the heart.

cardiovascular morbidity and mortality; thus, its analysis is needed.

VGStudio MAX 3.4 enables the user to calculate the total geometric volume of the voxels in selected region of interest (Table 3.6). Calculated numbers show that the muscle of the left ventricle has bigger volume than muscle of right ventricle. This corresponds to the fact that left ventricle has to pump oxygenated blood to the whole body whereas the right ventricle pumps blood to the lungs. The volumes for left and right ventricle are comparative.

| Anatomical part | Volume (mm^3) |
|-----------------|-------------------|
| RV - muscle | 1.36 |
| RV - air | 0.29 |
| LV - muscle | 1.70 |
| LV - air | 0.26 |
| RA - muscle | 0.63 |
| RA - air | 0.29 |
| LA - muscle | 0.41 |
| LA - air | 0.09 |
| Septum | 0.86 |

Table 3.6: Volumetric analysis of mouse heart E17.5 stained in PTA for 12 hours (RV - right ventricle, LV - left ventricle, RA - right atrium, LA - left atrium).

Wall thickness analysis

VGStudio visualisation software offers the Wall thickness analysis module that operates with voxel data set. The user can define the wall thickness interval and obtain a detailed colour-coded analysis of wall thickness. VGStudio offers two different methods: Ray and Sphere method. In the Ray approach, the wall thickness is measured by sending a perpendicular line from the current surface to the opposite. The endpoint on the

opposite side is considered within the specific search cone (a user defines aperture angle of the cone, Figure 3.14) [61].

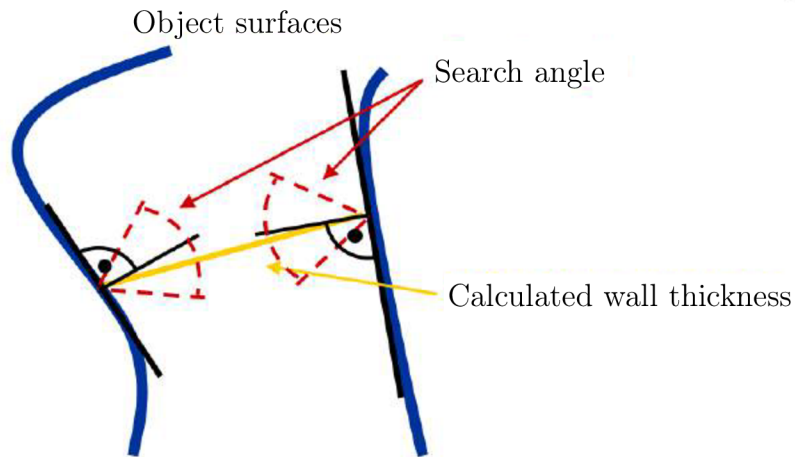


Figure 3.14: Search angle principle in the Ray method from VGStudio [61].

Figure 3.15 demonstrates the Ray method used for interventricular septum thickness analysis. The wall range was set from 0.00 to 1000.0 μm , and the angle search was evaluated for 15° and 30°. Even though the advance mode option was used to avoid gaps in the analysis, there are still some present. Therefore, the Ray method is not suitable for thick walls.

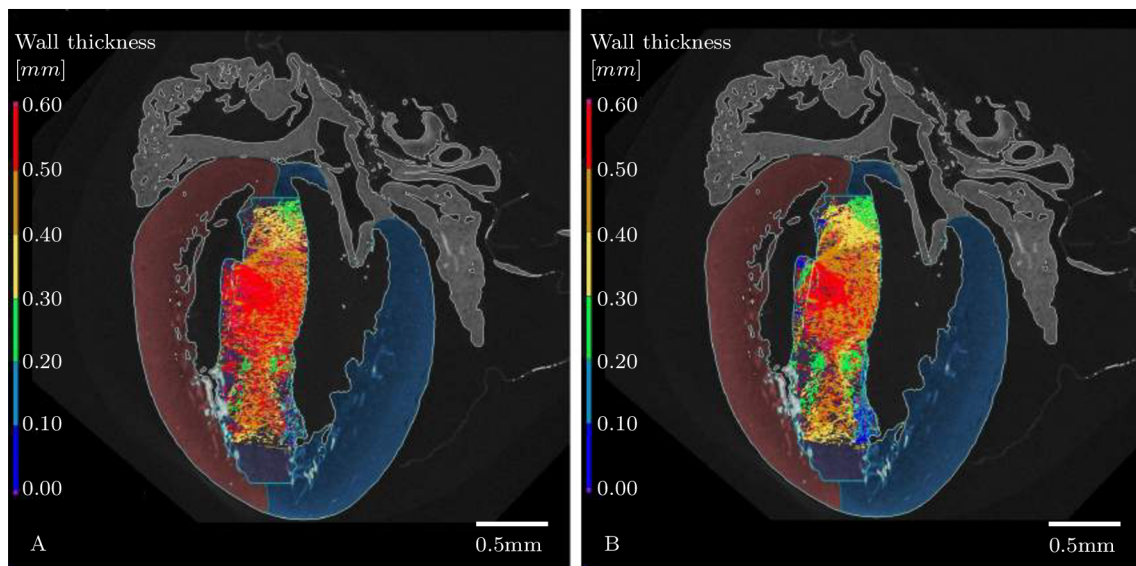


Figure 3.15: Wall thickness analysis of the IVS with ray method. Picture A: Search angle 15°, Picture B: Search angle 30°.

The Sphere method, explained in Figure 3.16, uses a principle of the rolling sphere to calculate the thickness. It starts from the current surface and expands until it interferes with the closest surface [63].

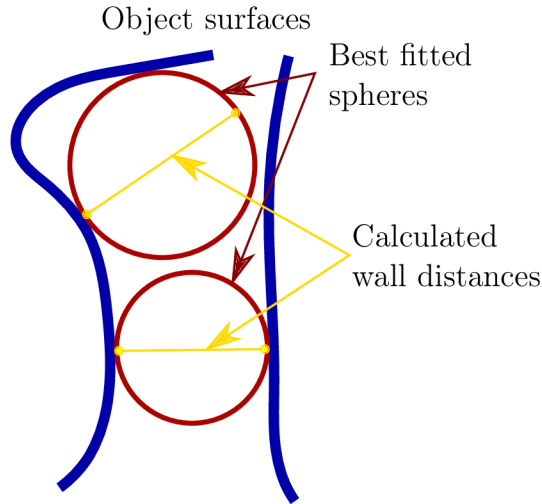


Figure 3.16: The sphere method principle.

The Sphere method provided better output than the Ray method for interventricular septum (Figure 3.17). Moreover, the result is without gaps but, regrettably, yields only an approximate description of thickness. The inaccuracy might be the result of an uneven surface or present holes in the structure. On the other hand, this method might be perfect for determining only the heart walls' muscular part without their trabecularities. To conclude, it is visible that the left ventricle wall is physiologically thicker than the right ventricle. The left ventricle has to pump blood through the whole body, whereas the right ventricle only to the lungs.

Nano CT evaluation of the heart septum

X-ray phase-contrast imaging provides additional information about the sample compared to conventional X-ray imaging (relying solely on absorption contrast). Phase-contrast imaging highlights the edges and internal boundaries of the specimen, and phase-shifting properties can be exploited to image low-density weakly absorbing 3D samples (with low atomic numbers). Therefore, it is perfect for imaging soft biological tissue and is promising a superior image quality and visibility of small features down to cellular level [35, 64]. Rigaku Nano3DX uses the Free-space propagation method to retrieve phase contrast which does not require any specialised elements [44].

Interventricular septum (IVS) was dissected from a wild type mouse heart E17.5 which was not stained with any high atomic chemicals. An unstained sample was chosen to show the ability of phase-contrast imaging to show edge enhancement at weakly absorbing samples. A small piece of tissue was embedded in a thin plastic tube with paraffin. Measurement was performed on a laboratory-based nano CT system Rigaku Nano3DX (Japan). The machine has a long source-detector distance (R_1) set to 260 mm (Figure 2.10). The projections were imaged on 3300×2500 px X-ray CCD camera with the pixel size $0.27 \mu\text{m}$. The binning 2 was used to achieve sufficient resolution (pixel size $0.54 \mu\text{m}$). The selected material for target was Cu, working at acceleration voltage 40 keV and tube current 30 mA , with the focal spot size $s = 73$

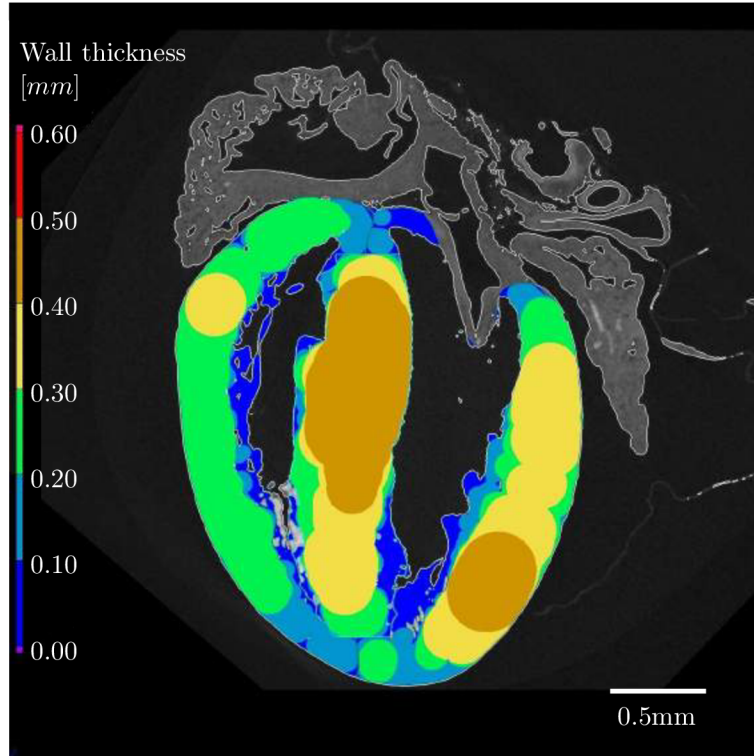


Figure 3.17: Wall thickness analysis of the right ventricle (left), septum (middle) and left ventricle (right) with sphere method.

μm . The range of sample rotation angle was 180° , the number of images was set to 800 and exposure time was 23 seconds. Total acquisition time was 5 hours and 36 minutes. According to Kalasova et al., to avoid geometrical unsharpness due to the finite focal spot size, the sample-detector distance (R_2) has to fulfil the equation, $R_2 < p \cdot R_1/s$. For the given values of R_1 (260 mm), p (pixel size, $0.54 \mu m$) and s ($73 \mu m$) the $R_2 = 1.923 mm$. For the calculated R_2 , 80 % of the maximal allowed distance was used = 1.7 mm. The coherence requirements are fulfilled for the equation $s \cdot R_2/a \cdot (R_1 + R_2) < 1$, considering the sample size 2 mm, $L_{shear}/L_{lat} = 0.005 < 1$. The image is magnified by the optical system placed after the detector [65]. Projections were reconstructed using VGStudio MAX 3.4 reconstruction module.

Evaluation of tomographic slices of the IVS from Figure 3.18 to show the influence of phase retrieval on CT data was done by plotting plot profiles, histograms and calculating CNR and SNR (contrast to noise ratio and signal to noise ratio, respectively). Figure 3.18, picture A, shows an absorption image with a pronounced edge enhancement at the borders between the sample and the air. Picture B is the same slice after application phase retrieval on tomographic data. The edge enhancement from picture A was plotted as a line profile (Figure 3.19, black line). After applying the phase retrieval, the edge enhancement was decreased (Figure 3.19, red line). The histogram of absorption contrast exhibit only one peak (Figure 3.20, black line). On the other hand, the histogram of data after phase retrieval has three peaks corresponding to different materials (air, paraffin, tissue). By counting the CNR and SNR values (according to equations 3.1 and 3.2, respectively) for absorption contrast data, $CNR =$

0.66, $\text{SNR} = 7.16$, and after application of phase retrieval technique, the both values rapidly increased, $\text{CNR} = 30.27$, $\text{SNR} = 69.83$.

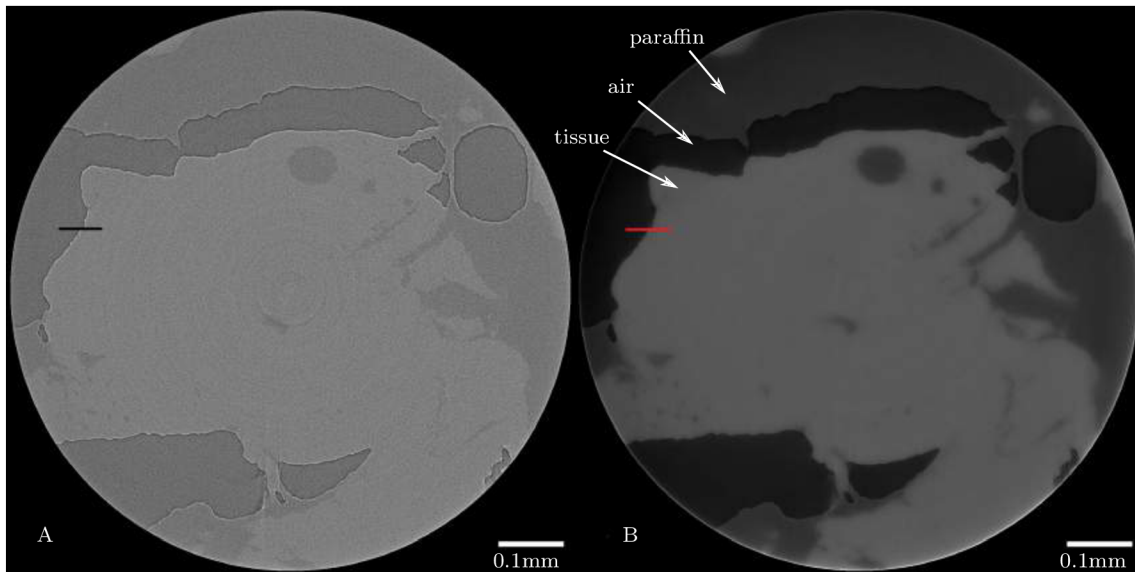


Figure 3.18: Tomographic slice of IVS without staining measured with Cu target, A: absorption contrast, B: slice with applied phase retrieval. The lines were used for plotting edge profiles.

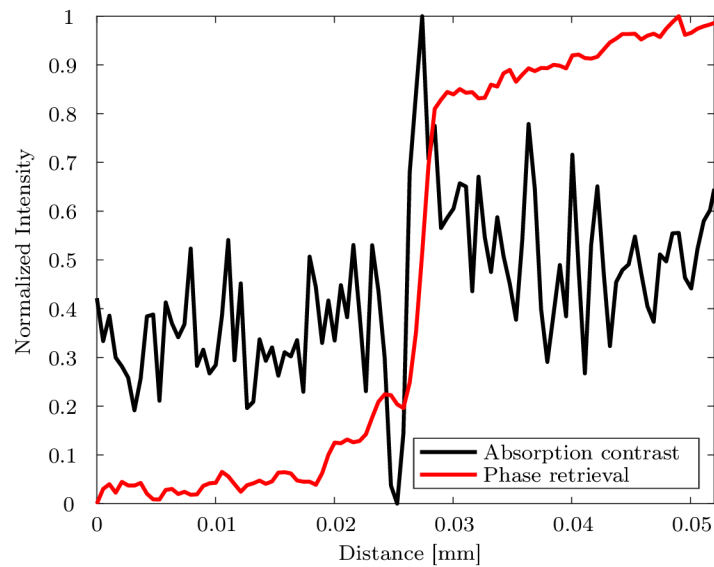


Figure 3.19: Edge profiles of data before (black line) and after application of phase retrieval algorithm (red line).

In the second experiment, the IVS was dissected from a PTA stained wild type heart E17.5 and embedded in 1% agarose gel to ensure proper fixation and avoid movement during longer scanning time. Imaging was also conducted in near-field regime ($N_F > 1$), $R_2 = 1 \text{ mm}$. It is necessary to use higher energy to image contrasted tissue; therefore, Mo target has been used, working at acceleration voltage 50 keV and

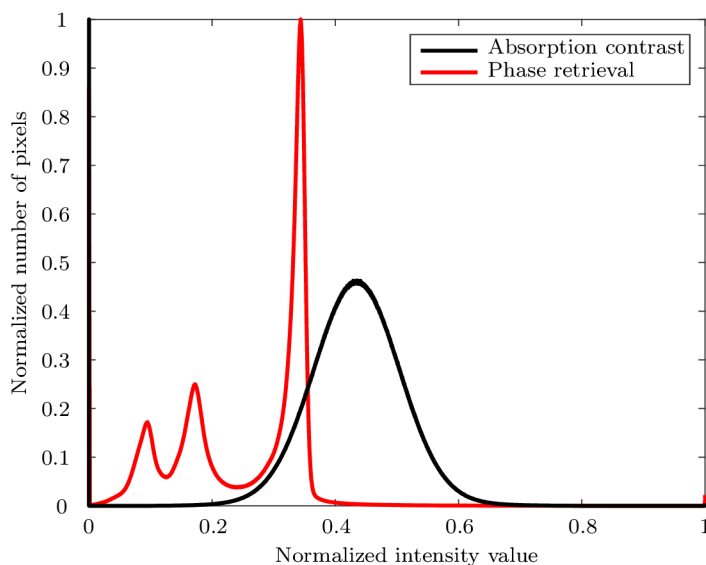


Figure 3.20: Histograms of data before (black line) and after application of phase retrieval algorithm (red line).

tube current 24 *mA*. The range of sample rotation angle was 180° , the number of images was set to 800 and exposure time was 40 seconds. Total acquisition time was 9 hours and 28 minutes. Figure 3.21 shows that stained tissue exhibits sufficient absorption contrast, and applying a phase retrieval algorithm does not provide improvement; moreover, the tissue structure is less discernible. Edge enhancement at agarose/tissue interface is less prominent than non-stained tissue (Figure 3.22). The histogram of tomographic slices for absorption contrast shows one small peak (agarose) and one tall peak (tissue) (Figure 3.23, black line). The histogram of the same data after applying phase retrieval has a similar shape with two main peaks, representing the same structures (Figure 3.23, red line). Even though the CNR and SNR values after application of the phase retrieval technique increased (CNR = 15.58, SNR = 34.67), compared to absorption contrast data (CNR = 4.81, SNR = 11.87), it is to less extent than after applying phase contrast to non-stained tissue. However, both values increased for absorption contrast in stained tissue. All values are presented in Table 3.7.

| | | |
|-------------------------------------|-------|-------|
| Tomographic data (without staining) | CNR | SNR |
| Absorption contrast | 0.66 | 7.16 |
| Phase retrieval | 30.27 | 69.83 |
| Tomographic data (with staining) | CNR | SNR |
| Absorption contrast | 4.81 | 11.87 |
| Phase retrieval | 15.58 | 34.67 |

Table 3.7: Values of CNR and SNR for IVS.

To conclude, phase contrast imaging expands the potential of X-ray computed nanotomography. Low absorbing biological samples benefited from substantial edge enhancement resulting in increased phase-contrast. Biological tissues stained with high

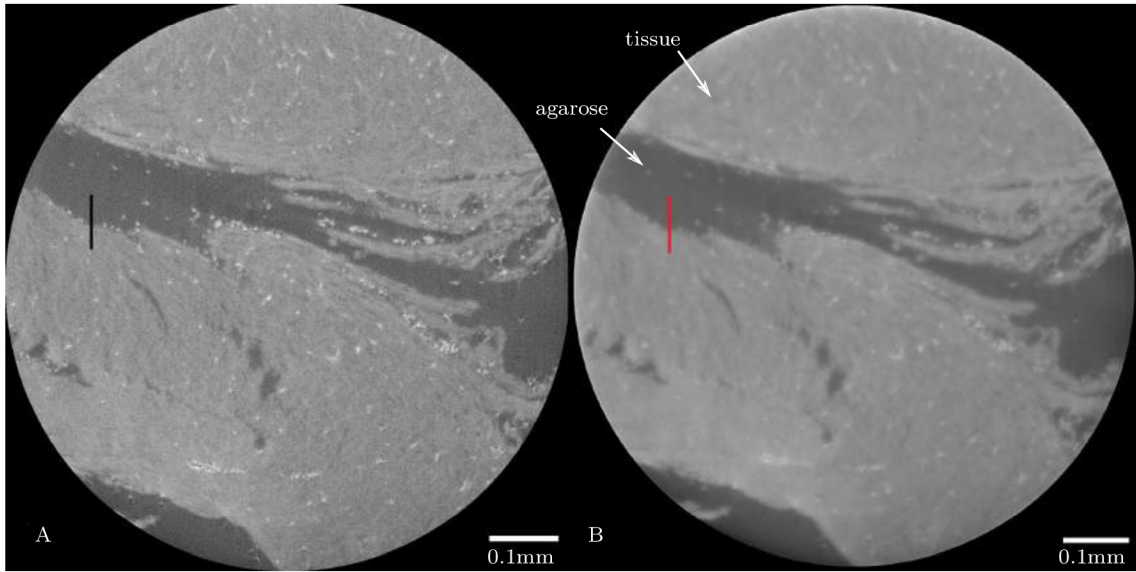


Figure 3.21: Tomographic slice of stained IVS measured with Mo target, A: absorption contrast, B: slice after applying phase retrieval. The lines were used for plotting edge profiles.

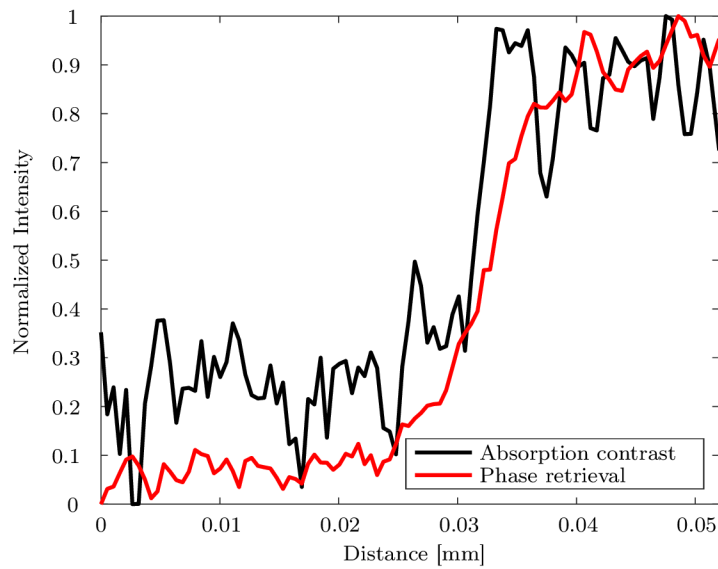


Figure 3.22: Edge profiles of data before (black line) and after application of phase retrieval algorithm (red line).

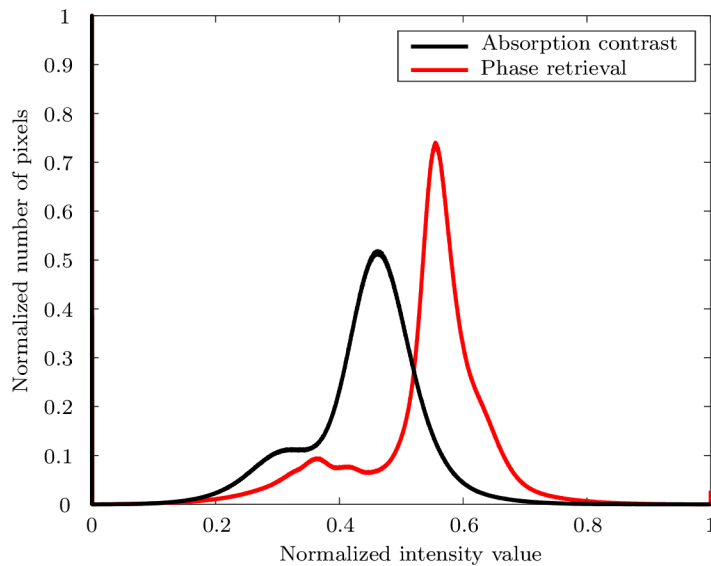


Figure 3.23: Histograms of data before (black line) and after application of phase retrieval algorithm (red line).

atomic elements provided excellent absorption contrast, enabling visualising the details of tissue structure. This experiment proved the tremendous potential of the staining procedure for μ CT and nano CT imaging of biological specimens.

3.3.4 Validation of the tomographic data with CLSM

Confocal laser-scanning microscopy (CLSM) provides high-resolution pictures; it can visualise internal structure by optical sectioning, and combined with fluorescent dyes, the cells can be imaged [66]. This technique is considered the gold standard in biology for cell research. However, as a conventional method, it offers only limited information regarding size, shape, extends and orientation of the whole studied structure. On the other hand, the innovative and non-destructive μ CT provides volumetric analysis of the 3D internal structures. Differences between CLSM and μ CT were shown and discussed with respect to sample preparation, measuring time, resolution, depth measurement ability in Chapter 3.3.

Oosterwyck et al. qualitatively evaluated CT's accuracy by comparing histological section with corresponding CT slices for the same position [46]. In this study, they used both techniques for characterising bone tissue around oral implants. The quantitative comparison of CLSM and CT method has been previously described by Kamburoğlu et al. [67]. They compared both methods by studying human maxillary incisor cavities, their diameter and volume. They examined the average diameters of cavities within one sample. Results obtained for both methods showed a strong positive correlation.

Aim of my work was to compare measurements obtained by μ CT with CLSM in interventricular septum (IVS) and use the potential of CLSM for validation of data from μ CT. For the histological section from the confocal microscope, the most corresponding CT slice was found (Figure 3.24). The correlation between the quantitative

measurements from μ CT and CLSM were tested by regression analysis. The null hypothesis H_0 says that between two sets of data does not exist statistically significant relation. Data were exported to Microsoft Excel, and the paired t-test was used to test this hypothesis with significance level $\alpha = 0.05$. If the $p < 0.05$, the null hypothesis was rejected. Table 3.8 shows measured distances of IVS retrieved by μ CT and CLSM, calculated average IVS thickness, standard deviation (SD) and maximum IVS diameter.

| Septum thickness [mm] | | |
|-----------------------|-------|-------|
| Num. | CT | CLSM |
| 1. | 0.547 | 0.539 |
| 2. | 0.549 | 0.567 |
| 3. | 0.569 | 0.537 |
| 4. | 0.569 | 0.556 |
| 5. | 0.571 | 0.551 |
| 6. | 0.570 | 0.571 |
| 7. | 0.561 | 0.524 |
| 8. | 0.546 | 0.485 |
| 9. | 0.520 | 0.408 |
| 10. | 0.484 | 0.404 |
| 11. | 0.463 | 0.416 |
| 12. | 0.456 | 0.389 |
| 13. | 0.454 | 0.383 |
| mean | 0.527 | 0.478 |
| SD | 0.046 | 0.071 |
| max | 0.571 | 0.571 |

Table 3.8: CT and CLSM values for septum thickness (Num. 1. to 13.), mean value for septum thickness, standard deviation (SD) and maximum value.

There is a significant relation in the measured IVS thickness between confocal microscopy and μ CT. The Figure 3.25 is showing very high positive correlation which is statistically important with significance level $\alpha = 0.05$ ($r = 0.921018$; $p = 0.001896$). Null hypothesis is rejected ($p < 0.05$).

To directly compare three-dimensional μ CT data with histology, the counterpart of the histological section has to be localised within the three-dimensional μ CT dataset. The data obtained from both methods originate from two samples (different animals) which might have some phenotype variation. Nevertheless, they were the same age, E17.5 and the same anatomical structure (interventricular septum) was analysed. It is clear that the microscope still has a much higher resolution, so quantitative measurements on histological sections will have a higher accuracy [46]. However, the 3D information provided by μ CT contributes a piece of priceless information to the research. μ CT has been previously proven to be a complementary method to the microscopic examination of tissue sections [47].

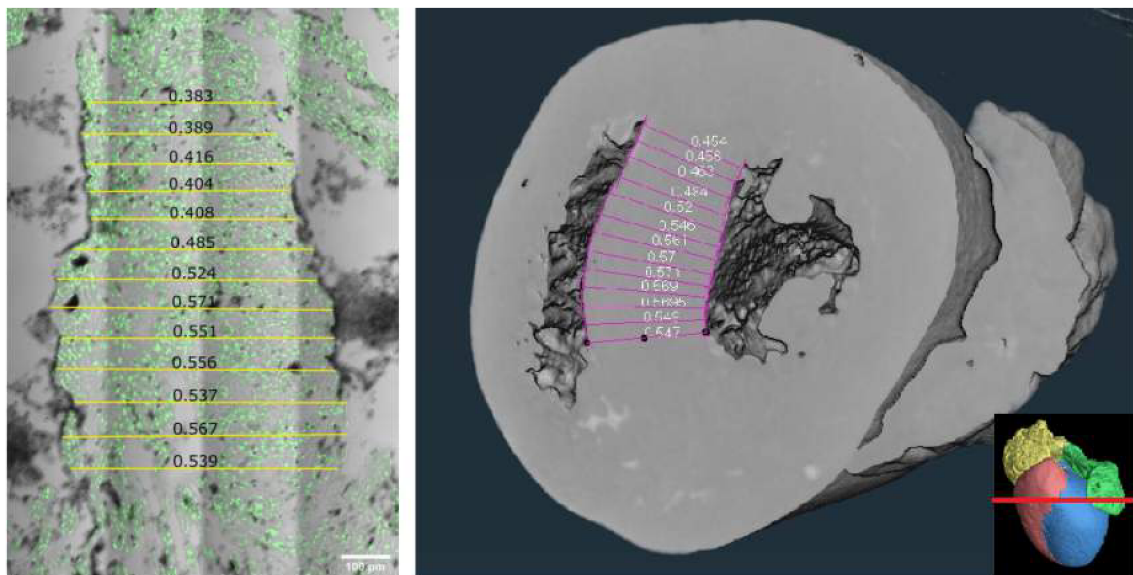


Figure 3.24: A transverse cut of mouse heart E17.5, Left picture: histological section of the interventricular septum from confocal laser scanning microscope (CLSM), Right picture: rendered volume of the whole heart cut in half. The measurements are in *mm*.

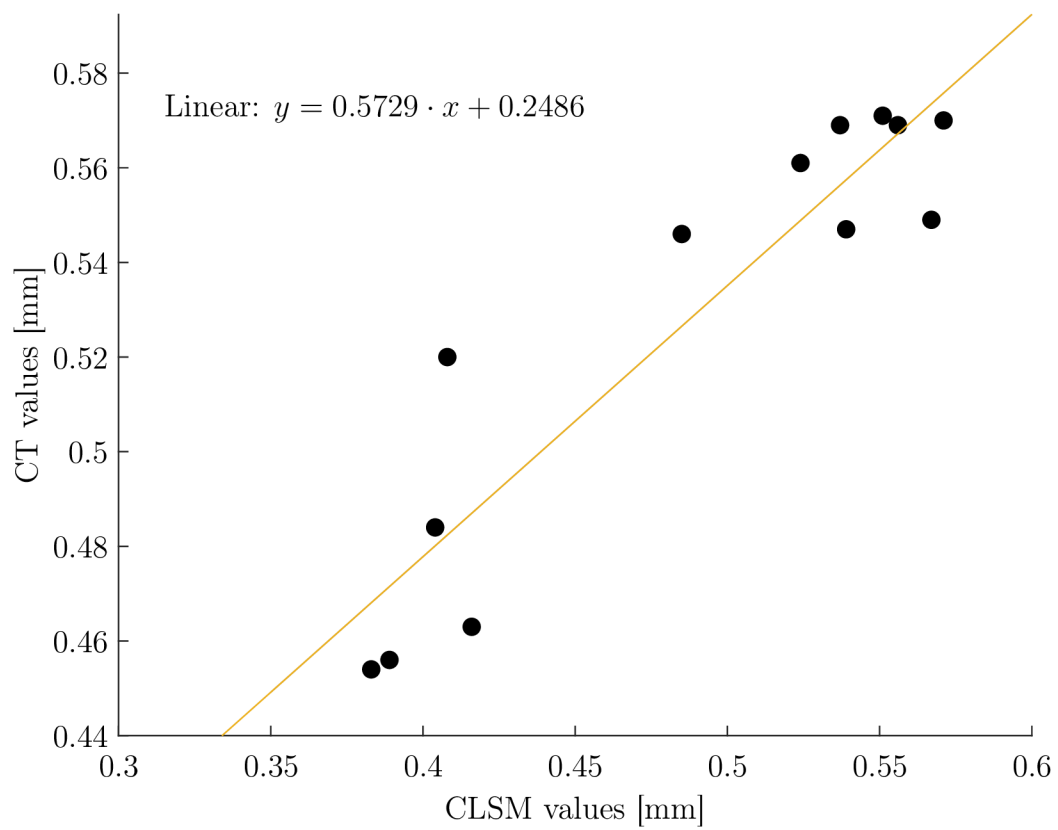


Figure 3.25: Regression analysis of CT and CLSM values for interventricular septum (IVS) thickness. The scattered plot shows the x-axis with CLSM values, the y-axis with CT values and the fitted OLS regression line.

3.3.5 Example on a mutant and a wild type

To show the proposed methodology for the segmentation of a control mouse heart (E17.5), mutant mouse NEUROGENIN 1 KO was selected. A knockout mouse (KO) has been used in developmental biology to distinguish the role of one targeted gene by its deletion. Therefore, these animal models are a valuable tool for modelling various human genetic diseases. Knockout mice can be used as a resource to study underlying pathophysiology and to develop therapies to treat a disease [68]. This thesis aims to show the methodology for the visualization of segmented 3D models. Due to the current ongoing situation, the accessibility of samples was limited. The specimens originate from two different laboratories, so there might be an age variation due to slightly different age recording. To adequately describe phenotype of NEUROGENIN 1 KO mice, further research with more samples should be conducted.

The mutant sample was stained with PTA contrast-enhancing agent, which was evaluated as the best contrast agent for small biological samples. The scan was done on GE phoenix v|tome|x L240 system with the same system settings as described in Chapter 3.2.4 and the same analysis was performed as for the wild type sample. Figures 3.26 and 3.27 show the pictures from volumetric analysis and wall thickness analysis of control and mutant embryonic heart, respectively. Table 3.9 shows comparison of volumetric analysis of control and mutant anatomical parts.

| Anatomical part | Volume Control (mm^3) | Volume Mutant (mm^3) |
|-----------------|---------------------------|--------------------------|
| RV - muscle | 1.36 | 0.38 |
| RV - air | 0.29 | 0.47 |
| LV - muscle | 1.70 | 0.51 |
| LV - air | 0.26 | 0.23 |
| RA - muscle | 0.63 | 0.50 |
| RA - air | 0.29 | 0.19 |
| LA - muscle | 0.41 | - |
| LA - air | 0.09 | - |
| Septum | 0.86 | 0.16 |

Table 3.9: Comparison of volumetric analysis of control and mutant mouse heart E17.5 (RV - right ventricle, LV - left ventricle, RA - right atrium, LA - left atrium).

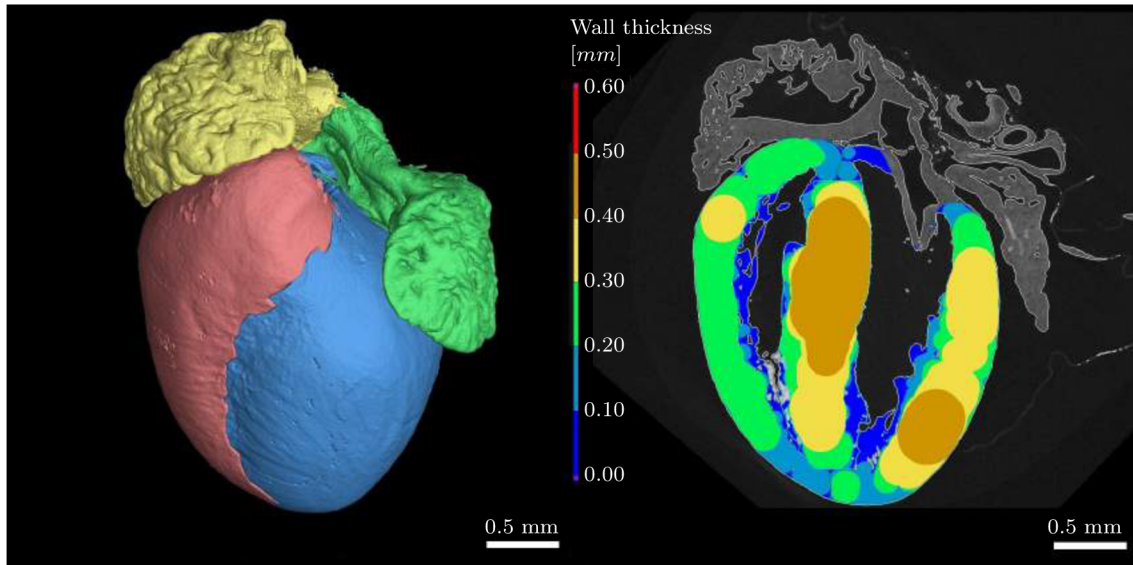


Figure 3.26: Control embryo.

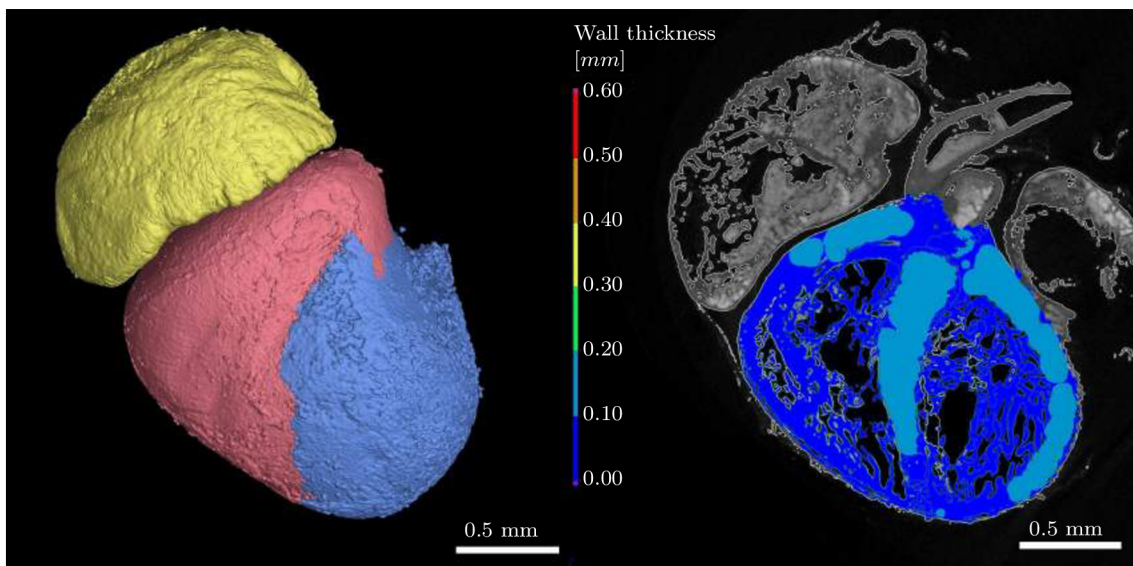


Figure 3.27: Mutant embryo.

Conclusion

This thesis deals with the analysis of the mouse embryonic heart (E17.5) using laboratory X-ray computed tomography. Mice are well-suited animals for modelling different diseases of the heart (atherosclerosis, cardiomyopathy, coronary heart diseases, myocardial infarction, congenital heart diseases, septal defects, anomalies in outflow tract and aortic arch), considering their very similar cardiac anatomy. However, mice with congenital heart diseases usually die prenatally, so the analysis of embryonic mouse heart was suggested.

The theoretical part of the master thesis is devoted to basic principles of X-ray computed tomography, analytical image reconstruction technique and challenges of imaging biological samples are discussed. One of the most common conventional method to image histological samples is confocal microscopy. Preparation of histological samples means cutting tissue into few micrometers thin sections. Thus, by invasive cutting, the lateral resolution in the third dimension is lost. On the other hand, this technique can visualise in sub-cellular resolution.

Non-destructive three-dimensional (3D) imaging is an excellent complement to volumetric morphological information on a microscopic level. However, in order to be able to gain sufficient absorption contrast for soft tissue, staining is necessary. After the discussion of contrasting agents, different staining protocols for mouse heart were suggested and evaluated. It was shown that PTA has proven to be the most suitable high atomic substance for contrasting small biological samples like a mouse heart.

The segmentation approach for the mouse heart was introduced, and volumetric analysis and wall thickness of 3D models were performed. Furthermore, Rigaku nano3DX was used to scan a small piece of mouse heart interventricular septum (IVS). With a specific setup, this device allows to apply phase-contrast imaging. The results have shown that low absorbing biological samples stained with PTA provided sufficient absorption contrast, which helped with the visualisation of details in the structure.

The tomographic data were validated with a confocal laser scanning microscope (CLSM). The counterpart of the prepared histological section has been localised within a 3D μ CT rendered volume. As a result, there was a significant relation between measured IVS thickness from CLSM and μ CT. Therefore, μ CT has been proven to be an equal method to the confocal microscope.

Finally, the suggested analysis was applied on a wild type mouse and mutant to demonstrate that the proposed methodology can be applied to mouse cardiac research in the future.

References

1. ANNUSVER, K.; WRIGHT, A. C.; HORNG, D.; PADMANABHAN, A.; EPSTEIN, J. A. Rapid 3D Phenotyping of Cardiovascular Development in Mouse Embryos by Micro-CT With Iodine Staining. *Circulation: Cardiovascular Imaging*. 2010, **3**(3), 314–322. Available from DOI: 10.1161/CIRCIMAGING.109.918482.
2. DOOST, A.; RANGEL, A.; NGUYEN, Q.; MORAHAN, G.; ARNOLDA, L. Micro-CT Scan with Virtual Dissection of Left Ventricle Is a Non-Destructive, Reproducible Alternative to Dissection and Weighing for Left Ventricular Size. *Scientific Reports*. 2020, **10**(1), 13853. ISSN 2045-2322. Available from DOI: 10.1038/s41598-020-70734-3.
3. NOVÁKOVÁ, M.; HAMPL, M.; VRÁBEL, D.; PROCHÁZKA, J. et al. Mouse Model of Congenital Heart Defects, Dysmorphic Facial Features and Intellectual Developmental Disorders as a Result of Non-Functional CDK13. *Frontiers in Cell and Developmental Biology*. 2019, **7**(155). ISSN 2296-634X. Available from DOI: 10.3389/fcell.2019.00155.
4. KIM, A. J.; FRANCIS, R.; LIU, X.; DEVINE, W. A. et al. Microcomputed Tomography Provides High Accuracy Congenital Heart Disease Diagnosis in Neonatal and Fetal Mice. *Circulation: Cardiovascular Imaging*. 2013, **6**(4), 551–559. Available from DOI: 10.1161/CIRCIMAGING.113.000279.
5. LEI, L.; SEOL, Y.; JARVIS, K. Pore-Scale Visualization of Methane Hydrate-Bearing Sediments With Micro-CT. *Geophysical Research Letters*. 2018, **45**(11), 5417–5426. ISSN 1944-8007. Available from DOI: 10.1029/2018GL078507.
6. KALASOVÁ, D.; ZIKMUND, T.; SPURNÝ, P.; HALODA, J., et al. Chemical and Physical Properties of Žďár Nad Sázavou L Chondrite and Porosity Differentiation Using Computed Tomography. *Meteoritics & Planetary Science*. 2020, **55**(5), 1073–1081. ISSN 1945-5100. Available from DOI: 10.1111/maps.13460.
7. KAVKOVA, M.; ZIKMUND, T.; KALA, A.; SALPLACHTA, J., et al. Contrast Enhanced X-Ray Computed Tomography Imaging of Amyloid Plaques in Alzheimer Disease Rat Model on Lab Based Micro CT System. *Scientific Reports*. 2021, **11**(1), 5999. ISSN 2045-2322. Available from DOI: 10.1038/s41598-021-84579-x.

8. KASTRITI, M. E.; STRATIGI, A.; MARIATOS, D.; THEODOSIOU, M., et al. Ablation of CNTN2+ Pyramidal Neurons During Development Results in Defects in Neocortical Size and Axonal Tract Formation. *Frontiers in Cellular Neuroscience*. 2019, **13**, 454. ISSN 1662-5102. Available from DOI: 10.3389/fncel.2019.00454.
9. BALTO, K.; WHITE, R.; MUELLER, R.; STASHENKO, P. A Mouse Model of Inflammatory Root Resorption Induced by Pulpal Infection. *Oral Surgery, Oral Medicine, Oral Pathology, Oral Radiology, and Endodontics*. 2002, **93**(4), 461–468. ISSN 1079-2104. Available from DOI: 10.1067/moe.2002.122641.
10. METSCHER, B. D. X-Ray Microtomographic Imaging of Intact Vertebrate Embryos. *Cold Spring Harbor Protocols*. 2011, **2011**(12), 1462–1471. ISSN 1559-6095. Available from DOI: 10.1101/pdb.prot067033.
11. METSCHER, B. D. MicroCT for Comparative Morphology: Simple Staining Methods Allow High-Contrast 3D Imaging of Diverse Non-Mineralized Animal Tissues. *BMC Physiology*. 2009, **9**(1), 11. ISSN 1472-6793. Available from DOI: 10.1186/1472-6793-9-11.
12. KALASOVÁ, D.; ZIKMUND, T.; PINA, L.; TAKEDA, Y., et al. Characterization of a Laboratory-Based X-Ray Computed Nanotomography System for Propagation-Based Method of Phase Contrast Imaging. *IEEE Transactions on Instrumentation and Measurement*. 2019, **69**(4), 1170–1178. Available from DOI: 10.1109/TIM.2019.2910338.
13. CIERNIAK, R. *X-Ray Computed Tomography in Biomedical Engineering*. England, United Kingdom: Springer Science & Business Media, 2011. ISBN 978-0-85729-027-4.
14. CHODOS, A. *November 8, 1895: Roentgen's Discovery of X-Rays* [online]. 2001-11 [visited on 2021-02-04]. Available from: <<http://www.aps.org/publications/apsnews/200111/history.cfm>>.
15. MIKLA, V. I.; MIKLA, V. V. *Medical Imaging Technology*. Saint Louis, UNITED STATES: Elsevier, 2013. ISBN 978-0-12-417036-0.
16. SUN, W.; BROWN, S. B.; LEACH, R. K. *An Overview of Industrial X-Ray Computed Tomography*. Hampton Road, Teddington, Middlesex, TW11 0LW, 2012. NPL Report, ENG 32. National Physical Laboratory. ISSN 1754-2987.
17. CARMIGNATO, S.; DEWULF, W.; LEACH, R. (eds.). *Industrial X-Ray Computed Tomography*. 1st. Springer International Publishing, 2018. ISBN 978-3-319-59573-3. Available from DOI: 10.1007/978-3-319-59573-3.
18. MAIER, A.; STEIDL, S.; CHRISTLEIN, V.; HORNEGGER, J. *Medical Imaging Systems: An Introductory Guide*. 1st ed. Switzerland: Springer International Publishing, 2018. ISBN 978-3-319-96520-8.
19. MACOVSKI, A. *Medical Imaging Systems*. 1st edition. Englewood Cliffs, N.J: Pearson, 1983. ISBN 978-0-13-572685-3.

20. ENDRIZZI, M. X-Ray Phase-Contrast Imaging. *Nuclear Instruments and Methods in Physics Research Section A: Accelerators, Spectrometers, Detectors and Associated Equipment*. 2018, **878**, 88–98. ISSN 0168-9002. Available from DOI: 10.1016/j.nima.2017.07.036.
21. HORNEGGER, J.; MAIER, A.; KOWARSCHIK, M. *CT Image Reconstruction Basics* [online]. 2018-10-07 [visited on 2021-02-24]. Available from: <<https://radiologykey.com/ct-image-reconstruction-basics/>>.
22. KAK, A. C.; SLANEY, M. *Computerized Tomographic Imaging*. New York: IEEE PRESS, 1987. ISBN 0-87942-198-3.
23. BOSCH MARIMON, M.; TORREJÓN - ESCRIBANO, B.; BOSCH RODRÍGUEZ, A.; CALVO ADEMUZ, M. Advanced Light Microscopy Techniques. *Scientific and Technological Centers. Barcelona University*. 2012.
24. LENG, Y. *Materials Characterization: Introduction to Microscopic and Spectroscopic Methods*. Weinheim, GERMANY: John Wiley & Sons, Incorporated, 2013. ISBN 978-3-527-67080-2.
25. TKACZYK, T. S. *Field Guide to Microscopy*. 1st. 1000 20th Street, Bellingham, WA 98227-0010 USA: SPIE, 2010. ISBN 978-0-8194-7246-5. Available from DOI: 10.1117/3.798239.
26. MATSUMOTO, B.; WRIGHT, S. J.; WRIGHT, D. J. *Cell Biological Applications of Confocal Microscopy*. 2nd edition. San Diego, California, USA: Academic Press, 2002. ISBN 978-0-08-049658-0.
27. DR. ROLF T. BORLINGHAUS. *Super-Resolution. On a Heuristic Point of View About the Resolution of a Light Microscope*. Leica Microsystems, 2014.
28. COGSWELL, C. J.; SHEPPARD, C. J. R. Confocal Differential Interference Contrast (DIC) Microscopy: Including a Theoretical Analysis of Conventional and Confocal DIC Imaging. *Journal of Microscopy*. 1992, **165**(1), 81–101. ISSN 1365-2818. Available from DOI: 10.1111/j.1365-2818.1992.tb04307.x.
29. LANG, W. Nomarski Differential Interference-Contrast Microscopy. *ZEISS Information*. 1968, **70**, 114–120.
30. LANG, W. Nomarski Differential Interference-Contrast Microscopy. II. Formation of the Interference Image. *ZEISS Information*. 1969, **71**, 12–16.
31. WEBER, M.; MICKOLEIT, M.; HUISKEN, J. Chapter 11 - Light Sheet Microscopy. In: WATERS, J. C.; WITTMAN, T. (eds.). *Methods in Cell Biology*. Academic Press, 2014, vol. 123, pp. 193–215. Quantitative Imaging in Cell Biology. Available from DOI: 10.1016/B978-0-12-420138-5.00011-2.
32. RAWSON, S. D.; MAKSIMCUKA, J.; WITHERS, P. J.; CARTMELL, S. H. X-Ray Computed Tomography in Life Sciences. *BMC Biology*. 2020, **18**(1), 21. ISSN 1741-7007. Available from DOI: 10.1186/s12915-020-0753-2.
33. STOCK, S. *Microcomputed Tomography: Methodology and Applications*. 1st. United States of America: CRC Press, 2008. ISBN 978-0-429-18674-5. Available from DOI: 10.1201/9780429186745.

34. TAKEYA, S.; MUROMACHI, S.; HACHIKUBO, A.; OHMURA, R., et al. X-Ray Attenuation and Image Contrast in the X-Ray Computed Tomography of Clathrate Hydrates Depending on Guest Species. *Physical Chemistry Chemical Physics*. 2020, **22**(47), 27658–27665. ISSN 1463-9084. Available from DOI: 10.1039/D0CP05466F.
35. REICHARDT, M.; TÖPPERWIEN, M.; KHAN, A.; ALVES, F.; SALDITT, T. Fiber Orientation in a Whole Mouse Heart Reconstructed by Laboratory Phase-Contrast Micro-CT. *Journal of Medical Imaging*. 2020, **7**(2), 023501. ISSN 2329-4302, ISSN 2329-4310. Available from DOI: 10.1117/1.JMI.7.2.023501.
36. DESCAMPS, E.; SOCHACKA, A.; KEGEL, B. D.; LOO, D. V., et al. Soft Tissue Discrimination with Contrast Agents Using Micro-CT Scanning. *Belgian Journal of Zoology*. 2014, **144**(1), 20–40. ISSN 2295-0451. Available from DOI: 10.26496/bjz.2014.63.
37. ZIKMUND, T.; NOVOTNÁ, M.; KAVKOVÁ, M.; TESAŘOVÁ, M., et al. High-Contrast Differentiation Resolution 3D Imaging of Rodent Brain by X-Ray Computed Microtomography. *Journal of Instrumentation*. 2018, **13**(02), C02039–C02039. ISSN 1748-0221. Available from DOI: 10.1088/1748-0221/13/02/C02039.
38. TESAŘOVÁ, M.; ZIKMUND, T.; KAUCKÁ, M.; ADAMEYKO, I., et al. Use of Micro Computed-Tomography and 3D Printing for Reverse Engineering of Mouse Embryo Nasal Capsule. *Journal of Instrumentation*. 2016, **11**(03), C03006–C03006. ISSN 1748-0221. Available from DOI: 10.1088/1748-0221/11/03/C03006.
39. DULLIN, C.; UFARTES, R.; LARSSON, E.; MARTIN, S. et al. CT of Ex-Vivo Stained Mouse Hearts and Embryos Enables a Precise Match between 3D Virtual Histology, Classical Histology and Immunohistochemistry. *PLoS ONE*. 2017, **12**(2), e0170597. ISSN 1932-6203. Available from DOI: 10.1371/journal.pone.0170597.
40. LESCIOTTO, K. M.; MOTCH PERRINE, S. M.; KAWASAKI, M.; STECKO, T., et al. Phosphotungstic Acid-Enhanced microCT: Optimized Protocols for Embryonic and Early Postnatal Mice. *Developmental Dynamics: An Official Publication of the American Association of Anatomists*. 2020, **249**(4), 573–585. ISSN 1097-0177. Available from DOI: 10.1002/dvdy.136.
41. METSCHER, B. D. MicroCT for Developmental Biology: A Versatile Tool for High-Contrast 3D Imaging at Histological Resolutions. *Developmental Dynamics*. 2009, **238**(3), 632–640. ISSN 1097-0177. Available from DOI: 10.1002/dvdy.21857.
42. KAUCKA, M.; ZIKMUND, T.; TESAROVA, M.; GYLLBORG, D., et al. *Oriented Clonal Cell Dynamics Enables Accurate Growth and Shaping of Vertebrate Cartilage*. eLife Sciences Publications Limited, 2017-04-17. Available from DOI: 10.7554/eLife.25902.
43. LIDER, V.; KOVALCHUK, M. X-Ray Phase-Contrast Methods. *Crystallography Reports*. 2013, **58**(6), 769–787. Available from DOI: 10.1134/S1063774513050064.

44. GUREYEV, T. E.; MAYO, S. C.; MYERS, D. E.; NESTERETS, Y., et al. Refracting Röntgen's Rays: Propagation-Based x-Ray Phase Contrast for Biomedical Imaging. *Journal of Applied Physics*. 2009, **105**(10), 102005. ISSN 0021-8979. Available from DOI: 10.1063/1.3115402.
45. CLERCQ, D. K.; PERSOONS, E.; NAPSO, T.; LUYTEN, C., et al. High-Resolution Contrast-Enhanced microCT Reveals the True Three-Dimensional Morphology of the Murine Placenta. *Proceedings of the National Academy of Sciences*. 2019, **116**(28), 13927–13936. ISSN 1091-6490. Available from DOI: 10.1073/pnas.1902688116.
46. VAN OOSTERWYCK, H.; DUYCK, J.; SLOTEN, J. V.; PERRE, G. V. et al. The Use of Microfocus Computerized Tomography as a New Technique for Characterizing Bone Tissue Around Oral Implants. *Journal of Oral Implantology*. 2000, **26**(1), 5–12. ISSN 0160-6972. Available from DOI: 10.1563/1548-1336(2000)026<0005:TUOMCT>2.3.CO;2.
47. KHIMCHENKO, A.; DEYHLE, H.; SCHULZ, G.; SCHWEIGHAUSER, G., et al. Extending Two-Dimensional Histology into the Third Dimension through Conventional Micro Computed Tomography. *NeuroImage*. 2016, **139**, 26–36. ISSN 1053-8119. Available from DOI: 10.1016/j.neuroimage.2016.06.005.
48. *Tissue-Tek® O.C.T. Compound* [online] [visited on 2021-03-22]. Available from: <<https://www.sakuraus.com/Products/Cryotomy/Tissue-Tek%C2%AE-O-C-T-Compound.html>>.
49. *Antigen Retrieval Solutions - Life Science Reagents for Immunohistochemistry (IHC)* [online] [visited on 2021-03-22]. Available from: <<https://www.sigmaldrich.com/programs/research-essentials-products.html?TablePage=110043770>>.
50. LI, Z.; CLARKE, J. A.; KETCHAM, R. A.; COLBERT, M. W.; YAN, F. An Investigation of the Efficacy and Mechanism of Contrast-Enhanced X-Ray Computed Tomography Utilizing Iodine for Large Specimens through Experimental and Simulation Approaches. *BMC Physiology*. 2015, **15**(1), 5. ISSN 1472-6793. Available from DOI: 10.1186/s12899-015-0019-3.
51. TAHARA, R.; LARSSON, H. C. E. Quantitative Analysis of Microscopic X-Ray Computed Tomography Imaging: Japanese Quail Embryonic Soft Tissues with Iodine Staining. *Journal of Anatomy*. 2013, **223**(3), 297–310. ISSN 0021-8782. Available from DOI: 10.1111/joa.12081.
52. TESAŘOVÁ, M. *Využití Průmyslové Rentgenové Počítačové Mikrotomografie ve Vývojové Biologii*. Brno, 2018. Vysoké učení technické v Brně. Fakulta strojního inženýrství.
53. KRAEMER, A.; KOVACHEVA, E.; LANZA, G. Projection Based Evaluation of CT Image Quality in Dimensional Metrology. In: *Digital Industrial Radiology and Computed Tomography*. Belgium, Ghent, 2015, pp. 22–25.
54. WEBB, S.; BROWN, N. A.; ANDERSON, R. H. The Structure of the Mouse Heart in Late Fetal Stages. *Anatomy and Embryology*. 1996, **194**(1), 37–47. ISSN 1432-0568. Available from DOI: 10.1007/BF00196313.

55. BOUKE A. DE BOER; GERT VAN DEN BERG; PIET A.J. DE BOER; MOORMAN, A. F.; RUIJTER, J. M. Growth of the Developing Mouse Heart: An Interactive Qualitative and Quantitative 3D Atlas. *Developmental Biology*. 2012, **368**(2), 203–213. ISSN 0012-1606. Available from DOI: 10.1016/j.ydbio.2012.05.001.
56. DESGRANGE, A.; LOKMER, J.; MARCHIOL, C.; HOUYEL, L.; MEILHAC, S. M. Standardised Imaging Pipeline for Phenotyping Mouse Laterality Defects and Associated Heart Malformations, at Multiple Scales and Multiple Stages. *Disease Models & Mechanisms*. 2019, **12**(7), dmm038356. ISSN 1754-8411. Available from DOI: 10.1242/dmm.038356.
57. WESSELS, A.; SEDMERA, D. Developmental Anatomy of the Heart: A Tale of Mice and Man. *Physiological genomics*. 2003, **15**, 165–76. Available from DOI: 10.1152/physiolgenomics.00033.2003.
58. WONG, M. D.; DORR, A. E.; WALLS, J. R.; LERCH, J. P.; HENKELMAN, R. M. A Novel 3D Mouse Embryo Atlas Based on Micro-CT. *Development*. 2012, **139**(17), 3248–3256. ISSN 1477-9129. Available from DOI: 10.1242/dev.082016.
59. SAVOLAINEN, S. M.; FOLEY, J. F.; ELMORE, S. A. Histology Atlas of the Developing Mouse Heart with Emphasis on E11.5 to E18.5. *Toxicologic pathology*. 2009, **37**(4), 395–414. ISSN 0192-6233. Available from DOI: 10.1177/0192623309335060.
60. KORNILOV, A. S.; SAFONOV, I. V. An Overview of Watershed Algorithm Implementations in Open Source Libraries. *Journal of Imaging*. 2018, **4**(10), 123. Available from DOI: 10.3390/jimaging4100123.
61. GMBH. *Volume Graphics*. VG, Heidelberg, Germany, 2016. VGStudio MAX 3.0.
62. BUTCHER, J. T.; SEDMERA, D.; GULDBERG, R. E.; MARKWALD, R. R. Quantitative Volumetric Analysis of Cardiac Morphogenesis Assessed through Micro-Computed Tomography. *Developmental Dynamics*. 2007, **236**(3), 802–809. ISSN 1097-0177. Available from DOI: 10.1002/dvdy.20962.
63. INUI, M.; UMEZU, N.; WAKASAKI, K.; SATO, S. Thickness and Clearance Visualization Based on Distance Field of 3D Objects. *Journal of Computational Design and Engineering*. 2015, **2**(3), 183–194. Available from DOI: 10.1016/j.jcde.2015.04.001.
64. MAYO, S. C.; STEVENSON, A. W.; WILKINS, S. W. In-Line Phase-Contrast X-Ray Imaging and Tomography for Materials Science. *Materials*. 2012, **5**(5), 937–965. ISSN 1996-1944. Available from DOI: 10.3390/ma5050937.
65. WALTON, L. A.; BRADLEY, R. S.; WITHERS, P. J.; NEWTON, V. L., et al. Morphological Characterisation of Unstained and Intact Tissue Micro-Architecture by X-Ray Computed Micro- and Nano-Tomography. *Scientific Reports*. 2015, **5**(1), 10074. ISSN 2045-2322. Available from DOI: 10.1038/srep10074.
66. SONDEJ, F.; BÜCK, A.; TSOTSAS, E. Comparative Analysis of the Coating Thickness on Single Particles Using X-Ray Micro-Computed Tomography and Confocal Laser-Scanning Microscopy. *Powder Technology*. 2016, **287**, 330–340. ISSN 0032-5910. Available from DOI: 10.1016/j.powtec.2015.09.039.

67. KAMBUROĞLU, K.; BARENBOIM, S. F.; ARITÜRK, T.; KAFFE, I. Quantitative Measurements Obtained by Micro-Computed Tomography and Confocal Laser Scanning Microscopy. *Dentomaxillofacial Radiology*. 2008, **37**(7), 385–391. ISSN 0250-832X. Available from DOI: 10.1259/dmfr/57348961.
68. HALL, B.; LIMAYE, A.; KULKARNI, A. B. Overview: Generation of Gene Knockout Mice. *Current Protocols in Cell Biology*. 2009, **Chapter 19**, 1–17. ISSN 1934-2616. Available from DOI: 10.1002/0471143030.cb1912s44.

List of abbreviations and symbols

| | |
|------------------|---|
| 1-D FT | one dimensional Fourier transform |
| 2-D FT | two dimensional Fourier transform |
| 2D, 3D | two-dimensional, three-dimensional |
| a | size of the sample |
| $a(x,y), b(x,y)$ | function of averaged background intensity, function of interference pattern intensity |
| A | atomic weight of the material |
| AU | Airy unit |
| APD | avalanche photo-diode |
| CCD | charge-coupled device |
| CI | Crystal interferometer |
| CLSM | confocal laser scanning microscope |
| CNR | contrast to noise ratio |
| CT | computed tomography |
| d | geometrical path |
| d_m | distance of a self-image of phase grating |
| DA | descending aorta |
| DEI | diffraction enhanced imaging |
| DIC | differential interference contrast |
| DICOM | Digital Imaging and Communications in Medicine |
| d_{xy} | lateral resolution |
| d_z | axial resolution |
| d_T | Talbot distance |
| eV | electron volt |
| F | fluorescent emission |
| $f(x,y)$ | function of an object in x,y coordinate system |
| $F(u,v)$ | 2-D FT of a projection $p(s,\theta)$ |
| FBP | filtered back projection |
| FWHM | full width at half maximum |
| G_0, G_1, G_2 | gratings in Talbot interferometer |
| HU | Hounsfield unit |
| Hz | Hertz |
| I | intensity of excitation light |
| $I(x,y)$ | intensity in x,y coordinate system |

| | |
|---------------------|---|
| I_0 | incident beam intensity |
| $I_0(E)$ | normalised energy spectrum |
| I_2 | iodine |
| I_t | transmitted beam intensity |
| IAS | interatrial septum |
| IVC | inferior vena cava |
| IVS | interventricular septum |
| keV | kilo electron volts |
| kV | kilo-volts |
| KO | knockout |
| l_c | spatial coherence |
| L_{shear} | shearing coherence |
| L_{lat} | lateral coherence |
| LA, RA | left and right atrium |
| LV, RV | left and right ventricle |
| LAA, RAA | left and right atrial appendages |
| LLL | Laue-Laue-Laue configuration interferometer |
| LSCV, RSCV | left and right superior caval vein |
| LSFM | light sheet fluorescence microscopy |
| m | metre |
| mA | miliampere |
| mm | millimetre |
| ms | milliseconds |
| n | refractive index |
| N_A | Avogadro's number |
| NA | numerical aperture |
| nanoCT, nCT | nano-computed tomography |
| N_F | Fresnel number |
| nm | nanometre |
| OsO_4 | osmium tetroxide |
| p | grating period, pixel size |
| $p(s, \theta)$ | function of a projection image |
| $P(\omega, \theta)$ | 1-D FT of a projection $p(s, \theta)$ |
| PBS | Phosphate Buffered Saline |
| PBST | Phosphate Buffered Saline, 0,1% Tween |
| PMT | photo-multiplier tube |
| PPC | propagation phase contrast |
| PSF | point spread function |
| PT | pulmonary trunk |
| PTA | phosphotungstic acid |
| px | pixel |
| Q | fluorophore quantum yield |
| r_e | classical electron radius |
| R1 | distance between source and object |

| | |
|---------------|--|
| R2 | distance between object and detector |
| s | distance from the origin of the coordinate system in the x,y plane, focal spot size |
| S, M, A | beam splitter, mirror, analyser |
| SEM | scanning electron microscopy |
| SNR | signal to noise ratio |
| SPIM | selective plane illumination microscopy |
| STL | STereoLitography |
| TEM | transmission electron microscopy |
| TI | Talbot interferometer |
| U | geometric unsharpness |
| u,v | coordinates in the frequency domain |
| UV | ultra-violet |
| x | length of X-ray path, material thickness |
| x,y | spatial coordinates in a plane perpendicular to the direction of radi- ation propagation |
| z | coordinate parallel to optical axis |
| Z | atomic number |
| z_{eff} | effective propagation distance |
| α | aperture angle, angle of deflected X-rays in TI method |
| β | absorption |
| δ | Dirac's function, phase shift |
| Δ | optical path |
| $\Delta(x,y)$ | phase shift introduced by imperfections of the interferometer |
| η | coefficient in Talbot distance |
| θ | angle from the x axis in the x,y plane, angle from the u axis in the frequency domain |
| λ | wavelength |
| μ | X-ray linear attenuation coefficient for homogeneous object [cm^{-1}] |
| μ_o | mean grey value of object |
| μ_B | mean grey value of background |
| $\mu(x)$ | X-ray linear attenuation coefficient for inhomogeneous object |
| μA | micro-ampere |
| μCT | micro-computed tomography |
| μm | micrometer |
| μ/ρ | mass attenuation coefficient [cm^2/g] |
| ρ | density [g/cm^3] |
| σ_B | noise in background |
| σ_o | noise in object |
| σ | molecular absorption cross-section |
| σ_S | standard deviation of the source intensity distribution |
| $\phi(x,y)$ | information about the phase |
| ω | angular frequency |
| $ \omega $ | filter function |

